Eastern Arctic Ocean Diapycnal Heat Fluxes through Large Double-Diffusive Steps

IGOR V. POLYAKOV

International Arctic Research Center, and College of Natural Science and Mathematics, University of Alaska Fairbanks, Fairbanks, Alaska

LAURIE PADMAN

Earth and Space Research, Corvallis, Oregon

Y.-D. LENN

School of Ocean Sciences, Bangor University, Menai Bridge, United Kingdom

ANDREY PNYUSHKOV AND ROBERT REMBER

International Arctic Research Center, University of Alaska Fairbanks, Fairbanks, Alaska

VLADIMIR V. IVANOV

Arctic and Antarctic Research Institute, St. Petersburg, and Lomonosov Moscow State University, Moscow, Russia

(Manuscript received 19 April 2018, in final form 1 November 2018)

ABSTRACT

The diffusive layering (DL) form of double-diffusive convection cools the Atlantic Water (AW) as it circulates around the Arctic Ocean. Large DL steps, with heights of homogeneous layers often greater than 10 m, have been found above the AW core in the Eurasian Basin (EB) of the eastern Arctic. Within these DL staircases, heat and salt fluxes are determined by the mechanisms for vertical transport through the high-gradient regions (HGRs) between the homogeneous layers. These HGRs can be thick (up to 5 m and more) and are frequently complex, being composed of multiple small steps or continuous stratification. Microstructure data collected in the EB in 2007 and 2008 are used to estimate heat fluxes through large steps in three ways: using the measured dissipation rate in the large homogeneous layers; utilizing empirical flux laws based on the density ratio and temperature step across HGRs after scaling to account for the presence of multiple small DL interfaces within each HGR; and averaging estimates of heat fluxes computed separately for individual small interfaces (as laminar conductive fluxes), small convective layers (via dissipation rates within small DL layers), and turbulent patches (using dissipation rate and buoyancy) within each HGR. Diapycnal heat fluxes through HGRs evaluated by each method agree with each other and range from ~2 to ~8 W m^{-2}, with an average flux of ~3–4 W m^{-2}. These large fluxes confirm a critical role for the DL instability in cooling and thickening the AW layer as it circulates around the eastern Arctic Ocean.

1. Introduction

Most of the oceanic heat entering the Arctic Ocean comes through Fram Strait in the Atlantic Water (AW) that then circulates as a warm boundary current along the continental slope of the eastern Arctic shelf seas (e.g., Aagaard 1989; Rudels et al. 1994). The maximum temperature of the AW decreases rapidly along this path, responding initially to direct ocean-to-atmosphere heat loss (e.g., Onarheim et al. 2014; Ivanov et al. 2012, 2016), then to mixing with cooler ambient waters from the continental shelves and in the deep basins (e.g., Walsh et al. 2007). The inferred average heat loss from the AW layer in the Nansen Basin, once it has subducted beneath the cold and relatively fresh Arctic Surface Water, is 4–6 W m^{-2} (Walsh et al. 2007; Polyakov et al. 2010). This value is large compared with the imbalance

Denotes content that is immediately available upon publication as open access.

Corresponding author: Igor Polyakov, ivpolyakov@alaska.edu

DOI: 10.1175/JPO-D-18-0080.1

of ~1 W m^{-2} required to explain decadal volume loss of the Arctic sea ice pack (Kwok and Untersteiner 2011; Carmack et al. 2015), suggesting that significant changes in the rate of heat loss from the AW layer could influence evolution of the sea ice.

Carmack et al. (2015) summarized the processes by which AW heat can be transported upward through the pycnocline above the AW layer. Two mechanisms—shear instabilities and double diffusion—are thought to be responsible for most diapycnal fluxes below the direct influence of stress and buoyancy forcing at the ocean surface. Shear instabilities associated with baroclinic tides and other tidally generated internal waves can lead to very large heat fluxes, with measured values sometimes greater than 10 and up to ~50 W m^{-2} (Padman and Dillon 1991; Rippeth et al. 2015), but these large fluxes appear to be localized near sources of baroclinic tides over the continental slope in the eastern Arctic (Padman 1995; Rippeth et al. 2015). It is not yet known how important shear instabilities are to AW heat transports when averaged over the entire Arctic Ocean. The second mechanism, double diffusion (Turner 1965, 1973), appears above the AW as the diffusive layering (DL) instability, which is known to be widespread throughout the Arctic Ocean (e.g., Timmermans et al. 2008; Rudels et al. 2009; Shibley et al. 2017). Peak measured heat fluxes from the DL instability are much lower than those due to shear instability; however, the basin-averaged contribution of the DL instability to heat loss from the AW core may exceed the contribution from tide-forced internal waves.

In this paper, we focus on the DL process in the eastern Arctic Ocean. The DL instability is described in detail by Kelley et al. (2003) and Radko (2013). When DL is active, vertical profiles of potential temperature θ and salinity S show a series of steps (called a "staircase") consisting of nearly homogeneous layers separated from each other by interfaces where θ and S change rapidly (Fig. 1b). Fluxes of heat, salt, and buoyancy are driven by the difference between the molecular diffusivities for temperature κ_T and salinity κ_S, where κ_T/κ_S is of order 100: rapid diffusion of the intrinsically unstable temperature component of total density at the edges of interfaces drives convection in the layers as described by Linden and Shirtcliffe (1978) and illustrated by Padman and Dillon (1987, their Fig. 7). More recent studies indicate that the process is more complex than these one-dimensional interpretations suggest. Carpenter et al. (2012) revealed that the transition to instability of a double-diffusive interface occurs as an oscillating diffusive convection mode at small boundary layer Rayleigh numbers, while nonlinear numerical simulations (Carpenter and Timmermans 2014) suggest that the convective plumes then organize into large-scale circulation cells.

Laboratory measurements (e.g., Marmorino and Caldwell 1976; Kelley 1990) and direct numerical simulations (Flanagan et al. 2013) show that the energetics of mixing and the magnitudes of the fluxes are functions of the change in potential temperature $\Delta\theta$ across an interface and the density ratio $R_\rho = (\beta\Delta S)/(\alpha\Delta\theta)$, where α and β are the thermal expansion and haline contraction coefficients, respectively, and ΔS is the salinity step across the interface. A value of $R_\rho = 1$ would indicate that the density change associated with the unstable temperature gradient exactly compensates the changes from the stabilizing salinity gradient. Values of $R_\rho > 1$ indicate the potential for the DL instability to be active. Laboratory experiments and numerical simulations demonstrate that for the same value of $\Delta\theta$, time-mean fluxes become larger as R_ρ decreases. Different parameterizations can differ by at least a factor of 2 in inferred heat fluxes (e.g., Kelley 1990; Robertson et al. 1995).

These so-called "flux laws," applied to hydrographic profiles from the eastern Eurasian Basin (EB), suggest heat fluxes of up to about 10 W m^{-2} (Lenn et al. 2009; Polyakov et al. 2012), with the largest values for DL steps just above the depth of the AW temperature maximum. These estimated DL heat fluxes are much larger than in the Canada Basin in the western Arctic, where values of order 0.1 W m^{-2} are typical (Padman and Dillon 1987; Timmermans et al. 2008). The applicability of laboratory-based flux laws to the more complex ocean has, however, been questioned (Padman 1994; Sirevaag and Fer 2012; Guthrie et al. 2015). Given the potential importance of DL heat fluxes to the large-scale heat budgets of the eastern Arctic Ocean above the AW layer, it is important to develop reliable flux parameterizations that are applicable to this oceanic region.

Two distinct classes of DL steps are found in the eastern Arctic: a few large layers, often >10 m high, separated by high-gradient regions (HGRs) with large values of $\Delta\theta$ and ΔS (e.g., between ~190 and 225 m in Fig. 1b); and sequences of several smaller steps with layers of order 1 m high and smaller values of $\Delta\theta$ and ΔS (e.g., above ~190 m in Fig. 1b). The thickness of HGRs can exceed 5 m, with complex internal structure that varies significantly between profiles (Fig. 2). Simultaneous measurements of hydrography and currents from a McLane moored profiler (MMP) record from the eastern Arctic slope (Polyakov et al. 2012) show that the horizontal velocity $\mathbf{U}(z)$ varies across large steps, with the largest shear magnitude tending to be coincident with DL interfaces and across HGRs (see example in Fig. 3). These observations are consistent with the interaction of mean, or slowly varying, sheared flow with the DL-driven processes of vertical transport of scalars and momentum described by Padman (1994).

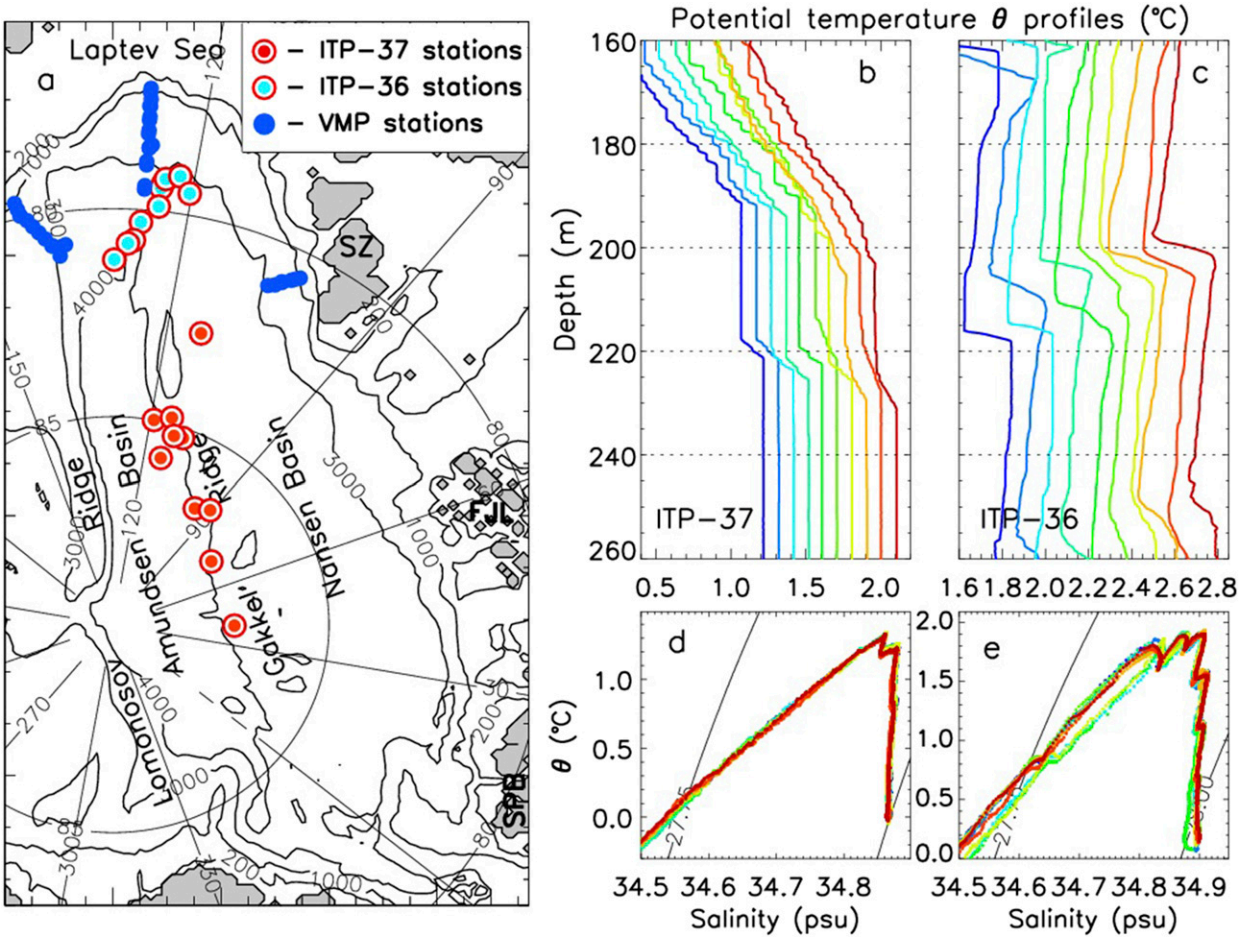

FIG. 1. (a) Map showing positions of selected ITP-36 (red/cyan) and ITP-37 (red/red) potential temperature θ profiles. Blue dots show locations of the 44 microstructure profiles made during 2007 and 2008 NABOS cruises and used in the present study. SZ, FJL, and SPB indicate Severnaya Zemlya, Franz Josef Land, and Spitsbergen. (b),(c) Example θ profiles from ITP-37 and ITP-36; 0.1°C offset and color are used to separate these profiles. Note that in (b), ITP-37 profiles contain a set of small steplike structures within the 160–190-m depth range, and thick convective layers separated by HGRs in the lower part of the water column. In (c), the zigzag structure is indicative of intrusions in the ITP-36 profiles. (d),(e) The θ–S (salinity) diagrams for the same profiles. The zigzag structure of the ITP-36 profiles in (c) above the AW core (defined as the maximum) results in peaks in the θ–S diagram, whereas no peaks are found above the AW core in the ITP-37 θ–S diagram.

For typical values of $\Delta\theta$ and R_ρ, flux laws suggest heat fluxes of order 10 W m^{-2} for the larger steps and in the range of 0.1–1 W m^{-2} for the smaller steps. The focus of this study is on heat fluxes across the larger steps since estimated fluxes and their uncertainties are large, and none of the previous studies of Arctic DL fluxes using microstructure data specifically focused on analysis of these features. Our analyses follow the general approaches applied to smaller steps by Sirevaag and Fer (2012) and Guthrie et al. (2015).

2. Data and methods

a. Summary of microstructure profiler observations

Microstructure observations were made during the 2007 and 2008 summer cruises of the Nansen and Amundsen Basins Observational System (NABOS) research program. About 80 profiles of temperature T, conductivity C, and microscale vertical shear of the horizontal current u_z to 600-m depth were collected in three cross-slope transects (Fig. 1a) using a Vertical Microstructure Profiler (VMP) manufactured by Rockland Scientific Instruments. These data have been described previously by Lenn et al. (2009, 2011) and Rippeth et al. (2015). We excluded profiles made in water less than 500 m deep to limit influence of shelf/slope processes. Of the remaining profiles, 44 contained high-quality records of all variables required for our analyses.

The VMP was deployed in tethered, free-fall mode with typical fall speeds of ~0.6 m s^{-1}. Microscale measurements of T, C, and u_z were obtained with an FP07 thermistor, SBE7–38 microconductivity, and two SPM38–1 airfoil shear probes, respectively, each recorded at 512 samples

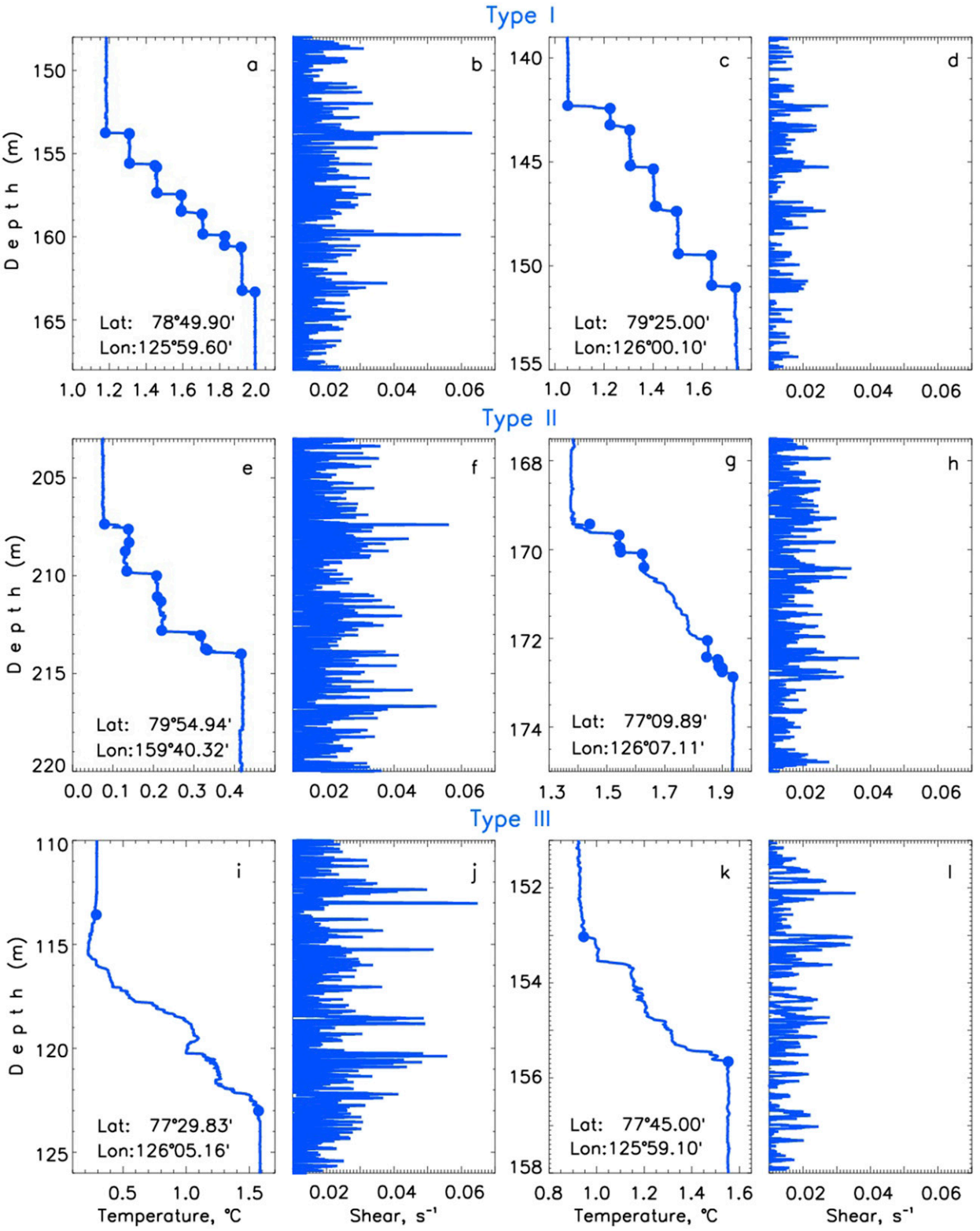

FIG. 2. Example profiles of microstructure temperature and vertical shear of horizontal currents containing large steps. (a)–(d) HGRs of Type I include a sequence of continuous small steps with no turbulent patches; (e)–(h) HGRs of Type II incorporate a mix of turbulent "noise" (turbulent patches) and several small steps; (i)–(l) HGRs of Type III lack well-developed small steps. Blue dots indicate ends of convective layers.

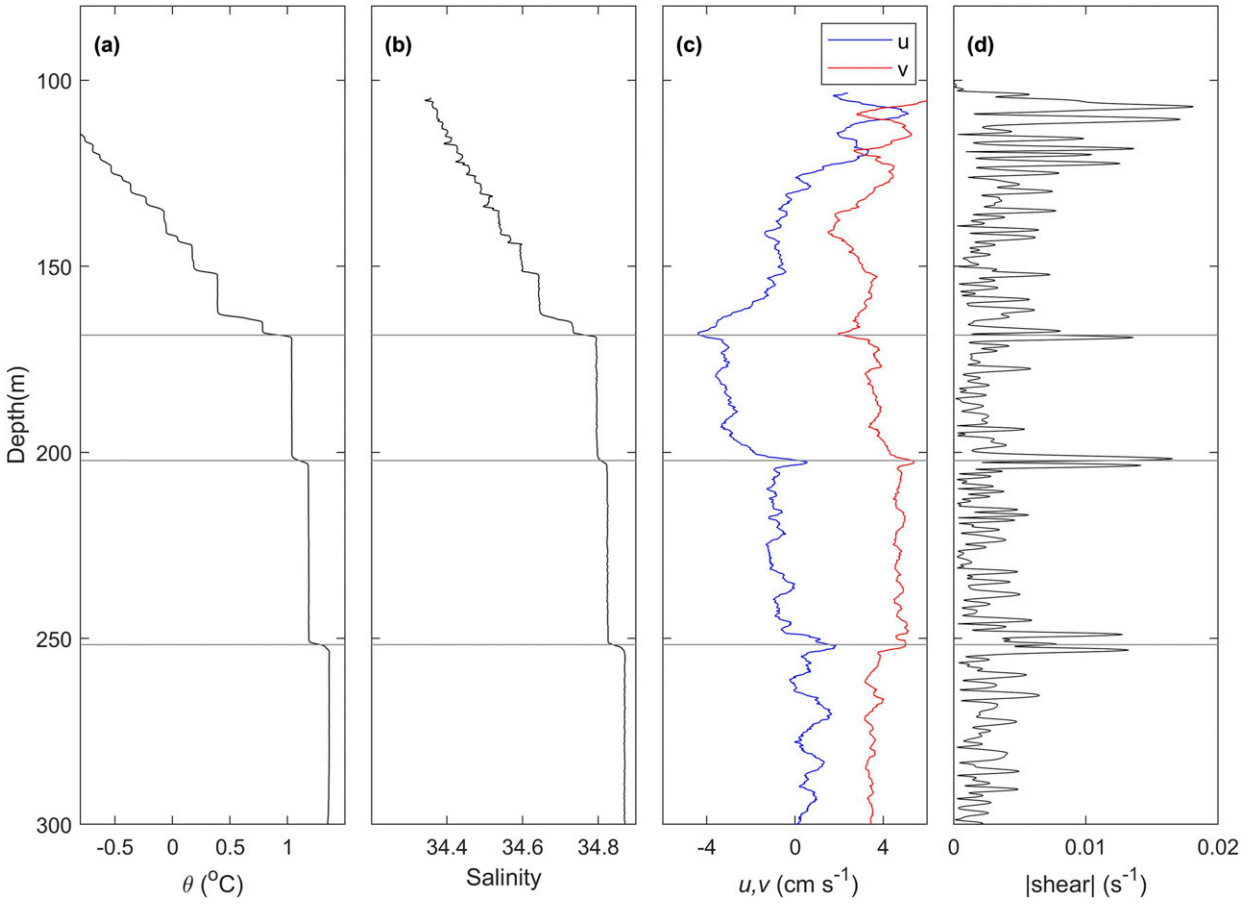

FIG. 3. Hydrographic and velocity profiles from a single profile from an MMP over the Laptev Sea slope [see Polyakov et al. (2012) for mooring details]. All data have been filtered to 1.5 m in the vertical. (a) Potential temperature θ; (b) salinity; (c) east u and north v components of velocity (cm s^{-1}); and (d) shear magnitude (s^{-1}). Horizontal gray lines on each panel mark the locations of three HGRs.

per second. A three-axis accelerometer provides high-frequency information on instrument tilt and vibrations that may be excited through the tether. The VMP was also equipped with a Seabird unpumped conductivity–temperature–depth (CTD) system (an SBE-3 thermistor and an SBE-4 conductivity cell), which provided much more accurate values of T and C but at much lower vertical resolution than the microstructure sensors. To identify the data sources for different analyses, we refer to data from the microstructure and Seabird sensors with subscripts "μ" and "SBE," respectively.

b. *Calibration of temperature and salinity*

Slow flow rates through the unpumped Seabird conductivity cell degraded the quality of C_{SBE} and S_{SBE} profiles. We therefore calibrated the VMP Seabird data with independent CTD measurements acquired by the Seabird SBE19plus CTD on the main ship system. The VMP casts followed immediately after the ship-based SBE19plus CTD casts were recovered during the 2007 and 2008 cruises, with the VMP casts taking about 30 min each. The VMP data were calibrated to the processed 1-dbar ship CTD data in T–S space to match extrema in water mass properties (i.e., AW intrusions, surface mixed layer temperature minima) while allowing for small isopycnal displacements between the CTD and VMP casts. This calibration process thus preserves the approximately 10-mm vertical sampling of the 64-Hz VMP Seabird data at a free-fall speed of 0.6 m s^{-1}. The CTD operations were based at the stern of the ship, while the VMP operations were based on the bow of the ship about ~150 m forward. We assume that the VMP was free-falling vertically from its drop position. The total separation of the VMP and CTD profiles is, therefore, a combination of the spatial separation of their deployments relative to the ship and the ship drift relative to the underlying water column during the 30 min between profiles. The ship SBE19plus CTD data were processed to reconcile the up- and downcast profiles at each station to produce 1-dbar (~1 m) resolution data. Our calibration

process ensures that the properties of the main water masses (i.e., mixed layer, halocline, and AW water) agree in T–S space and the 1-dbar data from the SBE19plus CTD was adequate to the task. Calibrated VMP Seabird data were used for the values of S_{SBE} reported here.

c. Resolution of microscale temperature sensor

The microstructure sensors provide much finer resolution of T and C than the Seabird sensors. For T_μ, the time constant of the FP07 double-pole response is roughly 10 ms (Sommer et al. 2013). At typical VMP fall speeds of $\sim 0.6\,\mathrm{m\,s^{-1}}$, this response corresponds to the ability to fully resolve scales of ~0.05 m (Gregg and Meagher 1980), much finer than can be resolved in CTD, MMP, and Ice-Tethered Profiler (ITP) profiles (~0.25–1 m) but still insufficient to fully resolve internal structure within small DL interfaces (Padman and Dillon 1987; Sommer et al. 2013; Guthrie et al. 2015).

d. Processing shear measurements and estimating dissipation rate ε

As the first step in processing microscale profiles of shear u_z, profiler motion was removed by deconvolving the shear signal with the accelerometer signal. Shear sensors on free-falling microstructure profiles measure u_z up to length scales set by the coupling of the profiler motion to the lateral flow: given the length of the VMP (~2 m), we expect that shear estimates between the sensor resolution (~0.03 m) and ~0.5–1 m should be resolvable, provided the shear signal is above the noise level. This band contains most of the shear variance that is expected in spectra for isotropic, fully developed turbulence for typical levels of turbulence in the present dataset. Noise beyond the accurately resolved vertical scales was removed from $u_z(z)$ using a 3–60-cm bandpass filter. The upper limit is smaller than the typical thickness of the HGRs between thick layers (Fig. 2); therefore, we cannot measure the large-scale shear magnitude $|\mathbf{U}_z|$ across HGRs that is sometimes seen in MMP profiles (Fig. 3).

Our principal use of microstructure shear profiles is calculation of the dissipation rate of turbulent kinetic energy ε (Gregg 1999). Assuming the turbulence is isotropic, the equation for fully developed isotropic turbulence (Kolmogorov 1941) is $\varepsilon = 7.5\nu\langle u_z^2\rangle\,\mathrm{W\,kg^{-1}}$, where ν is the kinematic viscosity of seawater ($\approx 1.8 \times 10^{-6}\,\mathrm{m^2\,s^{-1}}$ at 0°C), and angle brackets denote averaging over some depth interval, typically 0.5 m or greater. In many studies, the averaging depth interval is chosen to be constant. In DL staircases, however, the layers seen in hydrography provide the natural scale of vertical averaging. We use $\varepsilon_{\mathrm{LAYER}}$ to refer to dissipation rates calculated in large layers above and below HGRs and $\varepsilon_{\mathrm{layer}}$ to refer to rates within single DL layers within HGRs.

We used two methods for estimating $\langle u_z^2\rangle$. First, following Rippeth et al. (2003), we integrated the shear spectra between 2 and 30 cycles per meter (cpm). These integration limits were based on observed characteristics of shear spectra for a wide range of turbulence conditions and are consistent with the instrumentation; measured shear at wavenumbers less than 2 cpm is small because of coupling between the VMP and lateral flow, while the physical size of the shear sensor filters shear at wavenumbers greater than ~30 cpm. Second, we estimated $\varepsilon_{\mathrm{LAYER}}$ as an iterative best fit to the theoretical Panchev–Kesich spectrum of shear (Panchev and Kesich 1969; Gregg 1999) for fully developed turbulence. This approach minimizes issues associated with noise in individual shear spectra, but assumes that the true spectrum of shear at the time of measurement is correctly represented by the Panchev–Kesich spectrum. In our dataset, the values of $\varepsilon_{\mathrm{LAYER}}$ from the two methods are, in general, close to each other and correlated at $R = 0.82$.

For both approaches to estimating $\langle u_z^2\rangle$, the approximate noise floor for ε is $\varepsilon_{\mathrm{noise}} = 2 \times 10^{-10}\,\mathrm{W\,kg^{-1}}$, consistent with the value cited by Lenn et al. (2009). As discussed in section 3, this noise floor places significant constraints on the accuracy of variables, such as heat flux, derived from single estimates of ε. We estimated the uncertainty in ensemble means of fluxes by analyses of Monte Carlo simulations in which $\varepsilon_{\mathrm{noise}}$ is treated as a normally distributed random variable with standard deviation of $2 \times 10^{-10}\,\mathrm{W\,kg^{-1}}$ that is added to the set of measured values of ε, with the added condition that $\varepsilon \geq 0$. For typical sets of measured ε, the resulting uncertainty in ensemble means is primarily a function of the number of values in the ensemble, but is in the approximate range $0.2–0.6 \times 10^{-10}\,\mathrm{W\,kg^{-1}}$ for the ensemble sizes (14–48) considered here.

In further analyses, we used the estimates based on band-passed values. From measurements of $\varepsilon_{\mathrm{LAYER}}$, the approximate spread of values for the spectral fit for a specific band-passed estimate is about $\pm 1 \times 10^{-10}\,\mathrm{W\,kg^{-1}}$ (i.e., similar to the error associated with noise in shear).

Raw profiles of $u_z(z)$ can also be used directly to identify regions of high microscale shear (Padman 1994). However, as noted above, the long-wavelength cutoff caused by VMP coupling to the background velocity profile precludes calculation of background mean shear across thick HGRs.

e. Ancillary datasets

Microstructure observations were complemented by analysis of ship-based (mostly summer) CTD measurements and data from an MMP and drifting ITPs (www.whoi.edu/itp) providing year-round hydrographic measurements in the upper ~750 m. These MMP and ITP

measurements have accuracies of 0.002°C for temperature and 0.002 psu for salinity. The CTD SBE19plus V2 sensor has accuracies of 0.005°C for temperature and 0.0005 S m^{-1} for conductivity.

3. Results

a. Structure of large DL steps in the EB

From the 44 VMP microstructure profiles with good data for all needed variables and in water depths greater than 500 m, we identified 48 "large steps," defined as depth ranges with two well-mixed several-meters-thick layers separated by an HGR. We evaluated the temperature and salinity change ($\Delta\theta^{\mathrm{HGR}}$ and ΔS^{HGR}, respectively) across each HGR from the mean values of T_{SBE} and S_{SBE} in the adjacent two layers. The thickness of the HGR H^{HGR} was evaluated from the clearly defined upper and lower edges of the lower and upper layers (see Fig. 2 for examples). The density ratio (R_ρ^{HGR}) was evaluated using values of α and β based on the central values of T, S, and pressure P for the HGR.

For the 48 large steps, mean values of these variables were $\langle\Delta\theta^{\mathrm{HGR}}\rangle = 0.36$°C, $\langle\Delta S^{\mathrm{HGR}}\rangle = 0.06$, $\langle H^{\mathrm{HGR}}\rangle = 1.8$ m, and $\langle R_\rho^{\mathrm{HGR}}\rangle = 2.0$, respectively (Fig. 4). However, the probability distribution functions of $\Delta\theta^{\mathrm{HGR}}$, ΔS^{HGR}, and H^{HGR} are highly skewed so that their medians and means differ substantially, and we cannot define confidence intervals for the means. The distribution of R_ρ^{HGR} values is less skewed, and mean and median values are almost identical. The different types of HGR are found across broad ranges of $\Delta\theta^{\mathrm{HGR}}$ and ΔS^{HGR} (related through R_ρ^{HGR}), but there is no clear pattern to their relative distributions (Fig. 4e).

The average thickness of the 48 HGRs of $\langle H^{\mathrm{HGR}}\rangle = 1.8$ m is two orders of magnitude larger than the thickness of a few centimeters for typical single DL interfaces (e.g., Padman and Dillon 1987; Sommer et al. 2013, 2014; Guthrie et al. 2015). There are three distinct types of HGR seen in the VMP profiles of T_μ (Fig. 2), each representing about a third of the 48 steps. Fourteen of these HGRs consisted of a set of small and fairly uniform DL steps (Type I: Figs. 2a–d) that, individually, look similar to previously studied DL steps where the interfaces were assumed to be laminar (nonturbulent) with fluxes set by molecular diffusion (e.g., Padman and Dillon 1987; Sirevaag and Fer 2012; Carpenter and Timmermans 2014; Sommer et al. 2014; Guthrie et al. 2015). This type of HGR always contains at least five individual DL interfaces ($n \geq 5$). Seventeen HGRs consisted of a few sharp DL interfaces but with more thermal variability in some of the intervening low-gradient regions, and occasional patches with no discernible DL signals (Type II; $1 \leq n < 5$: Figs. 2e–h). These may be similar to Type I steps but with mixing of interfaces caused by shear from convectively driven eddies in the layers (Fernando 1989) or applied shear as reported by Padman and Dillon (1989) and Padman (1994). We refer to these segments of Type II HGRs as turbulent patches. The remaining 17 HGRs had either no small steps or just a hint of emerging small DL steps (Type III; Figs. 2i–l).

The range of HGRs may represent different stages of evolution from a common formation mechanism for large steps (see section 4) or intermittent response to changes in background forcing such as imposed shear (Fig. 3). The different characteristics suggest that the diapycnal heat, salt, and buoyancy fluxes may vary among HGRs that have similar bulk characteristics, as observed in coarsely resolved hydrographic profiles. For example, we expect that fluxes in a Type I HGR are driven entirely by the DL instability, so that the effective diapycnal diffusivity for salt K_S is much less than for temperature K_T (see, e.g., Kelley 1984). In contrast, these two diffusivities may be similar to each other in a Type III HGR if shear-driven mixing dominates; however, see Gargett (2003) for evidence that $K_S \neq K_T$ for some range of stratification and mixing rates when shear instability is the dominant mixing mechanism.

b. Relationship between DL structure and microscale shear

Peaks in profiles of the absolute value of microscale shear $|u_z|$ are frequently collocated with interfaces and HGRs [see the example profiles of temperature T_μ and $|u_z|$ in Figs. 2a–f and similar analyses by Padman (1994)]. Microscale shear at a single interface or HGR may result from several processes: externally imposed velocity structure (e.g., the large-scale geostrophic shear associated with mesoscale ocean state, and internal tides and other internal waves irradiating the steps; Padman and Dillon 1989; Padman 1994); the abrupt velocity difference associated with the eddy variability of velocities within the bounding quasi-homogeneous layers (Fernando 1987, 1989); and turbulence within the interface or HGR. In the case of externally imposed large-scale shear $\mathbf{U}_z$ (e.g., as seen in the MMP velocity profile in Fig. 3), we expect that the shear probes on the VMP would have recorded high microscale shear magnitudes across interfaces because the energetic, convectively driven turbulence in the adjacent layers homogenizes the horizontal velocity in each layer (Padman 1994). The second proposed source of high interfacial shear—eddy velocities associated with the DL-driven turbulence in the quasi-homogeneous layers—has been implicated in the increased diapycnal fluxes associated with values of R_ρ less than about 2 (e.g., Fernando 1987, 1989).

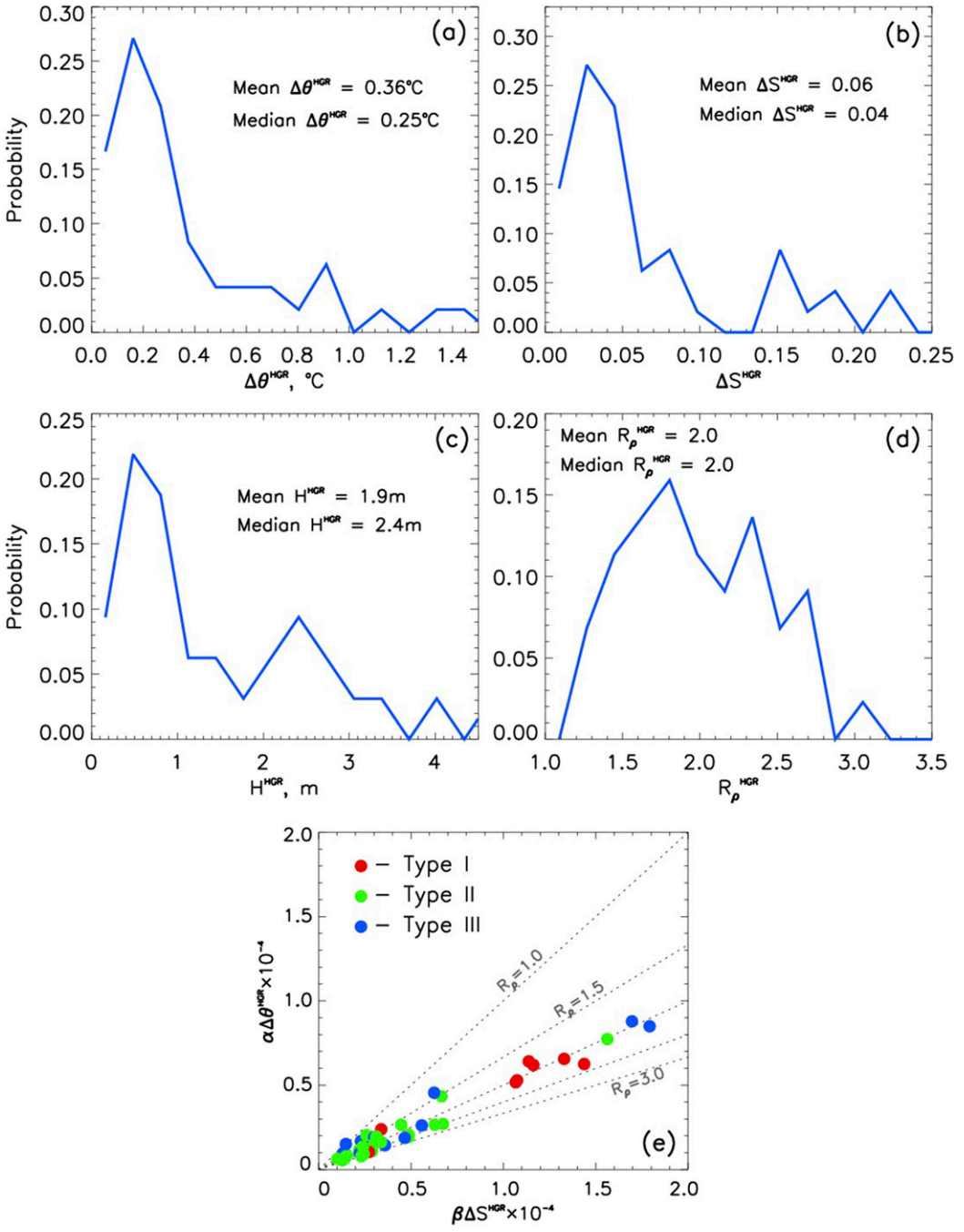

FIG. 4. Histograms of the (a) potential temperature change $\Delta\theta^{\mathrm{HGR}}$ and (b) salinity change ΔS^{HGR} across HGRs, (c) HGR thickness H^{HGR}, and (d) density ratio R_ρ^{HGR}. Mean and median values for each distribution are stated. (e) Relationship between $\alpha\Delta\theta^{\mathrm{HGR}}$ and $\beta\Delta S^{\mathrm{HGR}}$ (relative contribution to density change) color coded by interface type. Dotted lines show corresponding values of R_ρ^{HGR}.

We summarize the relationship between $|u_z|$ and location relative to HGRs by calculating, for each of the 48 large steps, the value of $|u_z|$ as a function of normalized distance z' from the bottom of the lower layer ($z' = 0$) to the top of the upper layer ($z' = 1$). The typical thickness of an HGR is about 10% of a complete step, and the two layers have similar thicknesses to each other; therefore, we assign the lower layer, HGR, and upper layer to the ranges $0 < z' < 0.45$, $0.45 < z' < 0.55$, and $0.55 < z' < 1$, respectively. We emphasize that the calculation of

$|u_z|(z')$ for each step is applied to microscale shear magnitude without regard to direction changes, and so is not directly comparable with the velocity and associated shear measurements from the MMP current meter profiles illustrated in Fig. 3. The mean profile of $|u_z|(z')$, averaged over all 48 large steps (Fig. 5), shows a clear maximum within the HGR ($0.45 < z' < 0.55$). The average value over the HGR is $0.013\,s^{-1}$ compared with $0.009\,s^{-1}$ in the upper and deeper convective layers; these estimates of means are statistically different from each other. Typical shear in an HGR is larger for Type II and Type III HGRs than for Type I HGRs (not shown).

c. *Heat fluxes through large DL steps in the EB*

The heat flux F_H through layers and adjacent HGRs in a single microstructure profile will not be the same, since the process of buoyancy production by diffusion at the edges of interfaces is intermittent (see section 1). Over a sufficiently long averaging time, however, vertical fluxes should be approximately continuous over some averaging time scale after lateral heat transport divergence along layers (Hieronymus and Carpenter 2016; Bebieva and Timmermans 2017) is taken into account. The heat flux through each step that we have identified can be estimated in three ways: from dissipation rates in the layers; from laboratory-based DL flux formulas; and from a weighted average of fluxes through small DL interfaces, DL layers, and turbulent patches within HGRs.

1) HEAT FLUX FROM LAYER DISSIPATION RATES

The turbulence in the well-mixed layers in DL steps is driven by the buoyancy flux F_b through the diffusive interfaces (e.g., Turner 1965, 1973; Linden and Shirtcliffe 1978; Taylor 1988). This net buoyancy flux is the sum of the destabilizing buoyancy flux due to heat $F_{bH} = (g\alpha/\rho c_P)F_H$ and the stabilizing salt flux F_{bS}, where g is the acceleration due to gravity, ρ is the density of seawater ($\sim 1030\,kg\,m^{-3}$), c_p is the specific heat of seawater ($\sim 3900\,J\,kg^{-1}\,K^{-1}$), and the salt flux is typically evaluated from a parameterized "buoyancy flux ratio" $R_F = F_{bS}/F_{bH}$. For $R_\rho > 2$, R_F is approximately constant near 0.15 (e.g., Turner 1965; Kelley 1990). The net buoyancy flux is upgradient. Note that the standard interpretation of shear-driven mixing assumes that the effective diapycnal diffusivities of heat and salt (K_T and K_S, respectively) are equal, so that R_F is given by $(\beta\partial S/\partial z)/(\alpha\partial T/\partial z) = R_\rho$, and the net buoyancy flux is downgradient.

Hieronymus and Carpenter (2016) evaluated a steady-state energy balance for DL staircases based on the Boussinesq approximation and a linear equation of state. Using their notation, this balance is

$$\langle F_b\rangle_{xy} = \langle \varepsilon_u\rangle_{xyz} + \langle F_b^{\rm cond}\rangle_{xyz}, \tag{1}$$

where $\langle F_b\rangle_{xy}$ is the average interfacial buoyancy flux, $\langle \varepsilon_u\rangle_{xyz}$ is the volume-averaged dissipation of kinetic energy, and $\langle F_b^{\rm cond}\rangle_{xyz}$ is the volume-averaged diffusive (conductive) buoyancy flux. These authors used direct numerical simulations to quantify this budget. In particular, they provided a ratio of $\langle \varepsilon_u\rangle_{xyz}$ and $\langle F_b^{\rm cond}\rangle_{xyz}$ for a range of values of the Rayleigh number

$$\mathrm{Ra} = \frac{g\alpha\Delta\theta H^3}{\upsilon k_T}, \tag{2}$$

where g is the acceleration due to gravity, and H is the thickness of DL convective layer. For typical values of $\Delta\theta^{\rm HGR}$ and $H^{\rm HGR}$ for our set of large DL steps, Ra is about 10^{11}, which is about three orders of magnitude greater than the maximum value of Ra of $\sim 10^8$ investigated by Hieronymus and Carpenter (2016). For that value of Ra, the ratio of $\langle \varepsilon_u\rangle_{xyz}$ to $\langle F_b^{\rm cond}\rangle_{xyz}$ is about 5–6. Although our Ra values imply that conductive heat and salt fluxes are negligible in the large Arctic DL steps discussed here, we included them in our energy balance estimates. Following Hieronymus and Carpenter (2016), and equating our measurements of dissipation in large layers ($\varepsilon_{\rm LAYER}$) to F_ρ (see below for further justification of this step), we obtain

$$\varepsilon_{\rm LAYER} + \frac{g}{H^{\rm LAYER}}(\alpha\kappa_T\Delta\theta + \beta\kappa_S\Delta S) = (1 - R_F)\frac{g\alpha}{\rho c_P}F_H^{\rm LAYER}. \tag{3}$$

The heat flux $F_H^{\rm LAYER}$ through large DL layers was estimated by inverting this expression. (Recall that we differentiate variables used for small DL layers found within HGRs vs variables used for large DL layers above and below HGRs by using lowercase "layer" vs uppercase "LAYER," respectively, as subscripts or superscripts.)

In the DL instability, turbulence in a layer is driven by the combined convective forcing of buoyant parcels formed at the upper edge of the lower interface and dense parcels formed at the lower edge of the upper interface. In a series of nonuniform steps, these sources of convection do not contribute equally to the layer turbulence level. This variability can drive a variety of processes including interface migration, layer splitting, and layer merging (Kelley et al. 2003). In our dataset, however, the estimates of $\varepsilon_{\rm LAYER}$ in the upper and lower layers were well correlated ($R = 0.73$), and their means were statistically indistinguishable (4.0 ± 0.5 and $4.1 \pm 0.6 \times 10^{10}\,W\,kg^{-1}$). For the present study, we

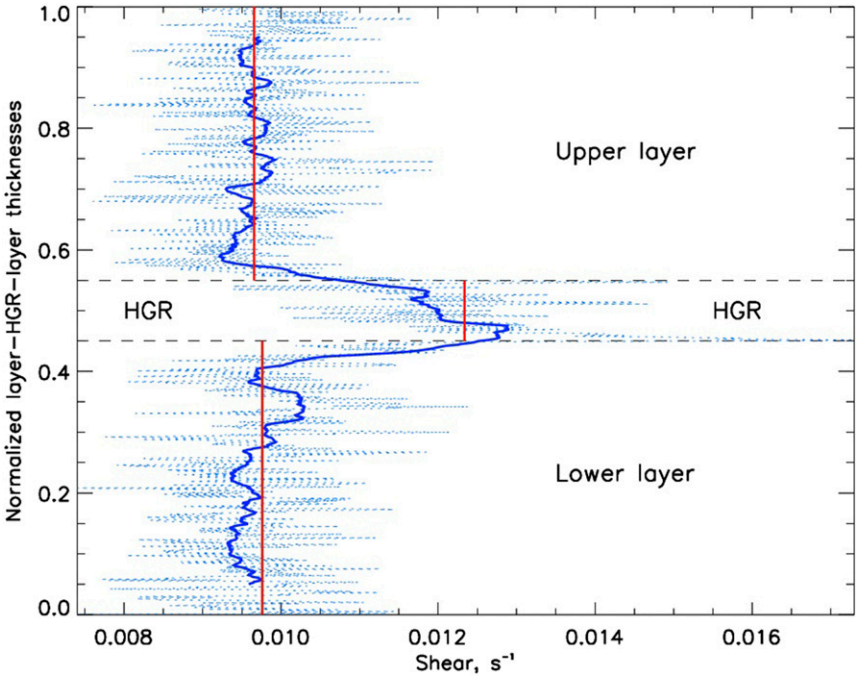

FIG. 5. Mean magnitude of microscale velocity shear within DL layers and HGRs, averaged over the 48 large steps. For each profile, the depth of each measurement of microscale shear magnitude was normalized to the range 0–1, where 0–0.45 is the lower layer, 0.45–0.55 is the HGR, and 0.55–1 is the upper layer. The blue dotted line is unsmoothed; the blue solid line is smoothed using a running mean of width 0.05 in normalized depth. Red segments show means for lower and upper DL layers and the HGR; the latter differs from layer means at the 95% confidence level.

use $\varepsilon_{\mathrm{LAYER}}$ derived from the averages of the layers above and below the HGR.

As Fig. 5 illustrates, the mean magnitude of microstructure shear (denoted $\langle|\mathrm{Sh}_{\mu}^{\mathrm{HGR}}|\rangle$) within HGRs exceeds values in the upper and lower layers. We found that $\varepsilon_{\mathrm{LAYER}}$ is strongly correlated ($R = 0.72$) with $\langle|\mathrm{Sh}_{\mu}^{\mathrm{HGR}}|\rangle$ within HGRs (Fig. 6), indicating that layers become more turbulent when shear in HGRs increases (note that correlation drops to $R = 0.59$ if the point with the highest values of $\varepsilon_{\mathrm{LAYER}}$ and $\langle|\mathrm{Sh}_{\mu}^{\mathrm{HGR}}|\rangle$ is removed). This correlation holds when large steps are sorted by type (Fig. 6), with $R = 0.70$ for Type I, $R = 0.65$ for Type II, and $R = 0.80$ for Type III. We do not have the concurrent measurements of large-scale velocity $\mathbf{U}(z)$ needed to determine the source of higher $\langle|\mathrm{Sh}_{\mu}^{\mathrm{HGR}}|\rangle$ in HGRs, although other measurements of $\mathbf{U}(z)$ through large DL steps (Fig. 3; Polyakov et al. 2012) suggest that layer turbulence may focus background imposed shear at interfaces and HGRs or provide the forcing for development of interfacial turbulence.

The associated heat fluxes across large layers F_H^{LAYER}, derived from layer dissipation rate [Eq. (3)], range from 2 ± 2 to $8 \pm 2\,\mathrm{W\,m^{-2}}$ (Fig. 6, right axis), where error bars represent the approximate uncertainty arising from an uncertainty of $2 \times 10^{-10}\,\mathrm{W\,kg^{-1}}$ in $\varepsilon_{\mathrm{LAYER}}$. The mean value is $3.6 \pm 0.5\,\mathrm{W\,m^{-2}}$ (Table 1), where the uncertainty was assessed following the procedure described in section 2d. This value of heat flux is comparable to the estimated loss from the AW layer in the eastern Arctic based on declining heat transport in the boundary current of AW (e.g., Carmack et al. 2015), confirming an important role for the DL instability in modifying AW layer properties.

2) HEAT FLUX ACROSS HGRS FROM DL FLUX LAWS

Estimates of heat flux for Type I and Type II HGRs (e.g., Figs. 2a–h) were derived from R_ρ and $\Delta\theta$ using the Kelley (1990) flux law applied to individual DL steps within the HGR, and to the full temperature step scaled by the number n of individual DL interfaces. The Kelley (1990) flux law is an empirical fit to laboratory measurements of DL fluxes, with the assumption that F_H is proportional to $\Delta\theta^{4/3}$ (e.g., Turner 1965, 1973) based on comparisons with heat transfer at solid conducting planes. However, the "4/3 flux law" assumes that the flux through an interface is independent of the thickness of the adjacent layers (i.e., that the convecting layers are

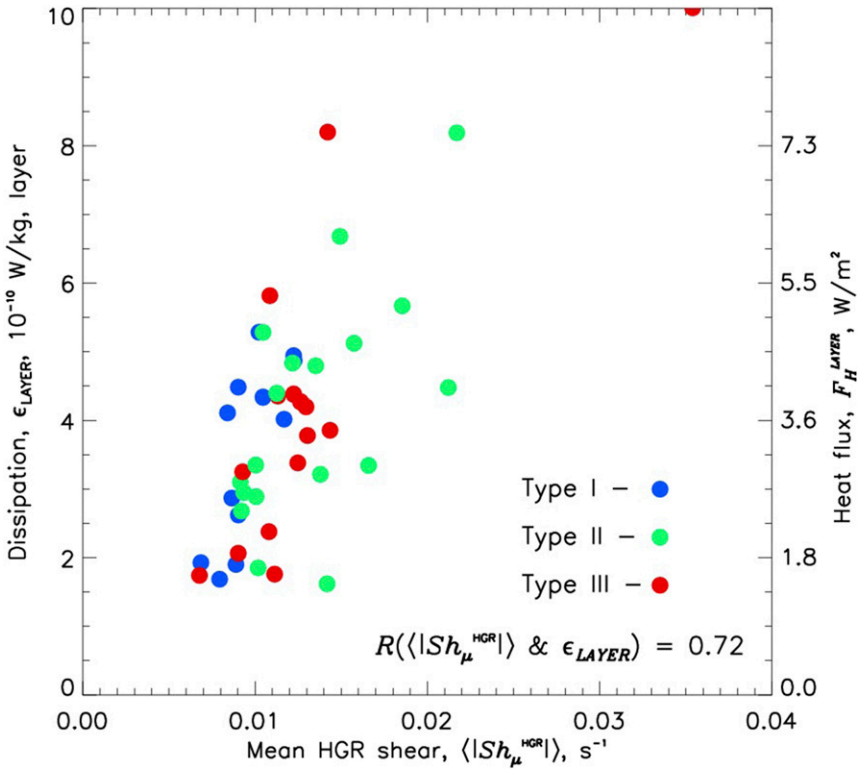

FIG. 6. Relationship between mean microscale velocity shear magnitude $\langle|\mathrm{Sh}_\mu^{\mathrm{HGR}}|\rangle$ and dissipation of turbulent kinetic energy in the thick convective layers $\varepsilon_{\mathrm{LAYER}}$, sorted by the HGR types. The correlation between $\varepsilon_{\mathrm{LAYER}}$ and $\langle|\mathrm{Sh}_\mu^{\mathrm{HGR}}|\rangle$ of $R = 0.72$ suggests a relationship between turbulence in the well-mixed layers and buoyancy flux through the HGRs resulting from either the DL instability or shear-driven turbulence.

sufficiently thick relative to the thickness of the interfaces; Turner 1965).

Variability in characteristics of individual interfaces within a single HGR leads to convergence or divergence of heat, salt, and buoyancy fluxes, thus altering the values of $\Delta\theta$ and R_ρ that would be applicable for future calculation of fluxes through individual interfaces. Given that our primary interest is in the long-term averaged fluxes associated with Arctic HGRs in large DL steps, we assume that the average flux through each interface in an HGR is identical such that diapycnal flux divergence is zero. We cannot, however, estimate whether layer splitting and merging, as discussed by Kelley et al. (2003) and others, might lead to rapid changes in n.

With the assumption of uniform DL fluxes through the individual interfaces in an HGR, we first calculated a heat flux $F_H^{\mathrm{HGR\text{-}lab}}$ based on the full value of $\Delta\theta$ between consecutive large layers (e.g., for the profile of θ_μ in Fig. 2a, we used $\Delta\theta \approx 0.8$°C). However, since this interface really consisted of $n = 7$ individual DL interfaces, the estimated heat flux should be scaled by $n^{4/3}$ (assuming equal interfaces), where the exponent of 4/3 comes from the DL flux laws. For this profile with $n = 7$, the factor $n^{4/3}$ reduced the estimated heat flux by a factor of ~13. The layer Rayleigh number $\mathrm{Ra}_{\mathrm{layer}}$ for individual layers within this HGR is about 10^8, which is comparable to values used in direct numerical simulations (Hieronymus and Carpenter 2016) and in laboratory measurements of DL (e.g., Kelley 1990; Kelley et al. 2003), suggesting that it is appropriate to apply the 4/3

TABLE 1. Heat fluxes (W m^{-2}) for all types of HGRs: shear-based F_H^{LAYER}; laboratory-based $F_H^{\mathrm{HGR\text{-}lab}}$ (see text for details); and HGR flux F_H^{HGR}, based on weighted fluxes for DL interfaces, DL layers, and turbulent patches. Ratios q_1 and q_2 compare F_H^{HGR} and $F_H^{\mathrm{HGR\text{-}lab}}$ to F_H^{LAYER}.

	Type I	Type II	Type III	All
F_H^{LAYER}	2.7 ± 0.7	3.0 ± 0.6	4.3 ± 1.6	3.6 ± 0.5
$F_H^{\mathrm{HGR\text{-}lab}}$	2.3 ± 0.6	2.0 ± 0.5	—	2.9 ± 0.4
$q_1 = F_H^{\mathrm{HGR\text{-}lab}}/F_H^{\mathrm{LAYER}}$	0.85	0.67	—	0.80
F_H^{HGR}	2.1 ± 0.5	3.1 ± 1.1	4.5 ± 1.0	3.3 ± 0.8
$q_2 = F_H^{\mathrm{HGR}}/F_H^{\mathrm{LAYER}}$	0.78	1.03	1.05	0.92

flux law at the level of individual interfaces. For a few individual steps within our sets of Type I and Type II HGRs, however, $\mathrm{Ra}_{\mathrm{layer}}$ is much smaller, of order 10^5, and layer thicknesses are the same order of magnitude as the measured thicknesses of interfaces (typically ~0.05–0.1 m). In these cases, the criteria underpinning the 4/3 flux laws are not met, and the processes driving fluxes through interfaces may be coupled with the secondary circulations within the layers. In the remainder of this discussion, we ignore this source of uncertainty in estimating fluxes through HGRs from flux laws. However, we note that a better understanding of flux dependence of $\Delta\theta$ on layer characteristics, as proposed by Kelley (1990), may be needed to understand evolution of DL layers as they evolve in time through merging and splitting, or emerge initially from larger-scale intrusions (Bebieva and Timmermans 2017).

For the set of 31 (Types I and II only) HGRs, n varied from 2 to 16, with three HGRs having $n \geq 10$. On average, $n \approx 4.8$. Estimates of R_ρ for individual DL interfaces within each high-gradient region were similar to each other and to the average for the entire large high-gradient region, indicating that the relationship between dS/dz and $d\theta/dz$ was fairly constant between the bounding upper and lower large layers. For the following analyses, we used $F_H^{\mathrm{HGR\text{-}lab}}$ scaled by $n^{4/3}$ for the estimate of interfacial heat flux. The uncertainties in these flux estimates depend almost entirely on the uncertainty in the flux law (see Robertson et al. 1995) since errors in R_ρ and $\Delta\theta$, which are both derived from the high-accuracy Seabird sensors on the VMP, are very small. Therefore, we do not include uncertainties in these fluxes.

The ratio q_1 of $F_H^{\mathrm{HGR\text{-}lab}}$ and heat flux in the adjacent large layers (F_H^{LAYER}) provides an estimate of the reliability of laboratory-based flux laws in this environment. An individual sample of an interface and its adjacent layers by microstructure profiler is not expected to yield an exact equivalence between $F_H^{\mathrm{HGR\text{-}lab}}$ and F_H^{LAYER} since the processes by which buoyant fluid is released from the interfaces to drive convection in the layers is intermittent (see, e.g., Padman and Dillon 1987; Hieronymus and Carpenter 2016). Nevertheless, mean heat fluxes show similar values for both approaches (Table 1). For Type I HGRs, $q_1 = 0.85$, suggesting validity of this approach for Type I interfaces, which are clearly dominated by active DL instability. The mean value of q_1 for Type II HGRs is further from unity, but still within the range of disagreement between different flux laws (Robertson et al. 1995).

3) Mixing in the stratified HGRs

Each HGR is composed of some combination of small DL interfaces, DL convective layers, and turbulent patches (Figs. 2, 3). Physical mechanisms driving heat transfer across these HGR segments differ, dictating different mathematical expressions for heat fluxes for these three segments of HGRs.

For sufficiently large R_ρ (greater than about 2, the mean value for HGRs discussed here), small DL interfaces are approximately laminar, with the conductive fluxes of heat and salt given by standard molecular (Fickian) diffusion:

$$F_H^{\mathrm{interface}} = \rho c_p \kappa_T \langle \partial\theta/\partial z \rangle_{\max}, \quad \text{and} \tag{4a}$$

$$F_S^{\mathrm{interface}} = \rho c_p \kappa_S \langle \partial S/\partial z \rangle_{\max}, \tag{4b}$$

where $\kappa_T = 1.4 \times 10^{-7}\,\mathrm{m^2\,s^{-1}}$ and $\kappa_S = 1.4 \times 10^{-9}\,\mathrm{m^2\,s^{-1}}$ are the molecular diffusivities of heat and salt, and $\langle \partial\theta/\partial z \rangle_{\max}$ and $\langle \partial S/\partial z \rangle_{\max}$ are the maximum potential temperature and salinity gradients within each interface (e.g., Padman and Dillon 1987; Guthrie et al. 2015). True values of $\langle \partial\theta/\partial z \rangle_{\max}$ may, however, be larger than the measured values, since the FP07 microstructure temperature sensor (section 2) cannot fully resolve thin interfaces at the typical fall speed ($0.6\,\mathrm{m\,s^{-1}}$) of the VMP. Using the Sommer et al. (2013, their Fig. 5) analyses of FP07 response characteristics as a function of fall speed, we find that the measured interface thickness h_i can exceed the true value by more than 20% for interfaces less than about 4 cm thick. For very thin interfaces, the relative error in thickness (and therefore gradient) can become very large.

Heat fluxes across small turbulent convective DL layers F_H^{layer} within HGRs were estimated using the same approach as we used for obtaining fluxes through large layers [Eq. (3)]:

$$\varepsilon_{\mathrm{layer}} + \frac{g}{H^{\mathrm{layer}}}[\alpha\kappa_T\Delta\theta + \beta\kappa_S\Delta S] = (1 - R_F)\frac{g\alpha}{\rho c_P} F_H^{\mathrm{layer}}. \tag{5}$$

Heat fluxes across turbulent patches F_H^{patch} (including HGRs with no small DL steps; i.e., Type III HGRs) were estimated following the general approach originally suggested by Osborn (1980) for estimating an effective diapycnal diffusivity K_ρ within a stratified fluid, using the average dissipation rate ε and mean buoyancy-frequency-squared $\langle N^2 \rangle$. Osborn (1980) found that for shear-driven turbulence,

$$K_\rho = \Gamma\varepsilon/\langle N^2 \rangle, \tag{6}$$

where Γ is a mixing efficiency (see below). Assuming the effective diffusivity for heat is the same as for buoyancy, the heat flux is then estimated as

$$F_H^{\text{patch}} = \rho c_p K_\rho \langle \partial\theta/\theta z \rangle, \quad (7)$$

where $\langle \partial\theta/\partial z \rangle$ is the mean vertical gradient of potential temperature.

This "mixing efficiency" approach was developed originally for shear-driven turbulence (i.e., mixing created by nonlinear processes such as Kelvin–Helmholtz and Holmboe instabilities; Turner 1973). A typical value of Γ for shear-driven turbulence is ~0.2 (e.g., Gregg 1987). Inoue et al. (2007) proposed that the approach could be extended to cases, such as the DL instability, where buoyancy flux is the driving force. Those authors found that in buoyancy-driven flows, the data fit to Eq. (7) suggested that $\Gamma \approx 1$. This value of Γ was confirmed by Hieronymus and Carpenter [2016, their Eq. (14)] through analyses of the equations of motion with simplifications appropriate to the DL instability.

The choice of $\Gamma \approx 1$ for mixing patches within Type II interfaces is reasonable, given the dominance of the DL instability. For Type III HGRs, we evaluated the optimum value of Γ by comparing F_H^{layer} with F_H^{patch} from Eq. (7). These fluxes are equal when $\Gamma \approx 1$ (Table 1), suggesting that fluxes through Type III HGRs are still dominated by buoyancy-driven processes.

We computed averaged interfacial heat flux (averaging indicated by $\langle\ \rangle$) as a weighted sum of fluxes $F_H^{\text{interface}}$ across all individual DL interfaces with thicknesses $H^{\text{interface}}$ within the HGR:

$$\langle F_H^{\text{interface}} \rangle = \left(\sum F_H^{\text{interface}} H^{\text{interface}}\right) / \sum H^{\text{interface}}. \quad (8)$$

We used similar formulas for estimating averaged heat fluxes across individual small DL layers F_H^{layer} and turbulent patches F_H^{patch} within the HGR. The total heat flux across each HGR F_H^{HGR} was then computed as a weighted average of fluxes across DL interfaces, layers, and turbulent patches:

$$F_H^{\text{HGR}} = \frac{\left(\langle F_H^{\text{interface}} \rangle \sum H^{\text{interface}} + \langle F_H^{\text{layer}} \rangle \sum H^{\text{layer}} + \langle F_H^{\text{patch}} \rangle \sum H^{\text{patch}}\right)}{H^{\text{HGR}}}. \quad (9)$$

The rationale for this approach is that we are attempting to estimate the *time-averaged* fluxes associated with HGRs. For a single microstructure profile, estimates of fluxes for single categories (layer, interface, turbulent patch) may vary substantially from each other even though, in a time-averaged sense, the vertical flux of heat is continuous through the entire HGR (associated lateral flux divergence is small). The weighting in Eq. (9) is, therefore, an attempt to use vertical *spatial* averaging of instantaneous fluxes to reduce uncertainty in the time-averaged values.

Estimated fluxes were strongest in turbulent patches (mean 3.6 W m^{-2}), somewhat weaker in convective layers (mean 3.5 W m^{-2}), and the weakest across DL interfaces (mean 1.5 W m^{-2}; Fig. 7), although the latter may be underestimated through underresolving temperature gradients with the FP07 thermistor on the VMP (Sommer et al. 2013). Type III HGRs (Fig. 2c) that are composed solely of turbulent patches yield the strongest heat fluxes (Table 1). Recall that for Type III HGRs, flux is linearly dependent on the choice of Γ, so that our choice of $\Gamma = 1$ is an upper bound on fluxes.

Uncertainties in estimates for heat fluxes in small DL layers and turbulent patches depend on the noise in measurements of shear that lead to the uncertainties in ε. In contrast, uncertainties in $F_H^{\text{interface}}$ depend only on the ability of the FP07 microstructure temperature sensor to resolve interfacial gradients $\partial T_\mu/\partial z$, with the values in Fig. 7 being lower limits on DL fluxes. These results support the view that the larger fluxes evaluated for DL layers are reasonable, even though they are only a factor of about 2 larger than the heat flux equivalent to the formal noise estimate for $\varepsilon^{\text{layer}}$ (see section 2d).

Fluxes for individual components in the calculation of net HGR heat flux decline with an increase in the number of small DL steps n, as quantified by negative trends of heat fluxes (Fig. 7). Note that elimination of points associated with the highest n (=15) does not change the result: negative trends still dominate. Although the strongest fluxes are found across the individual turbulent patches, convective DL layers represent the thickest segment of HGRs of Type I and Type II, and as a result, their overall contribution to heat flux across HGRs for these two types is the greatest (Fig. 7). In addition, the computed conductive component of F_H^{layer} [second and third terms of the left-hand side of Eq. (5)] is two to three orders of magnitude smaller than dissipation $\varepsilon_{\text{layer}}$. As a result, adding these terms has negligible effect on the overall estimates of F_H^{layer}.

The comparison of HGR fluxes from this approach with the concurrent values derived from $\varepsilon_{\text{LAYER}}$,

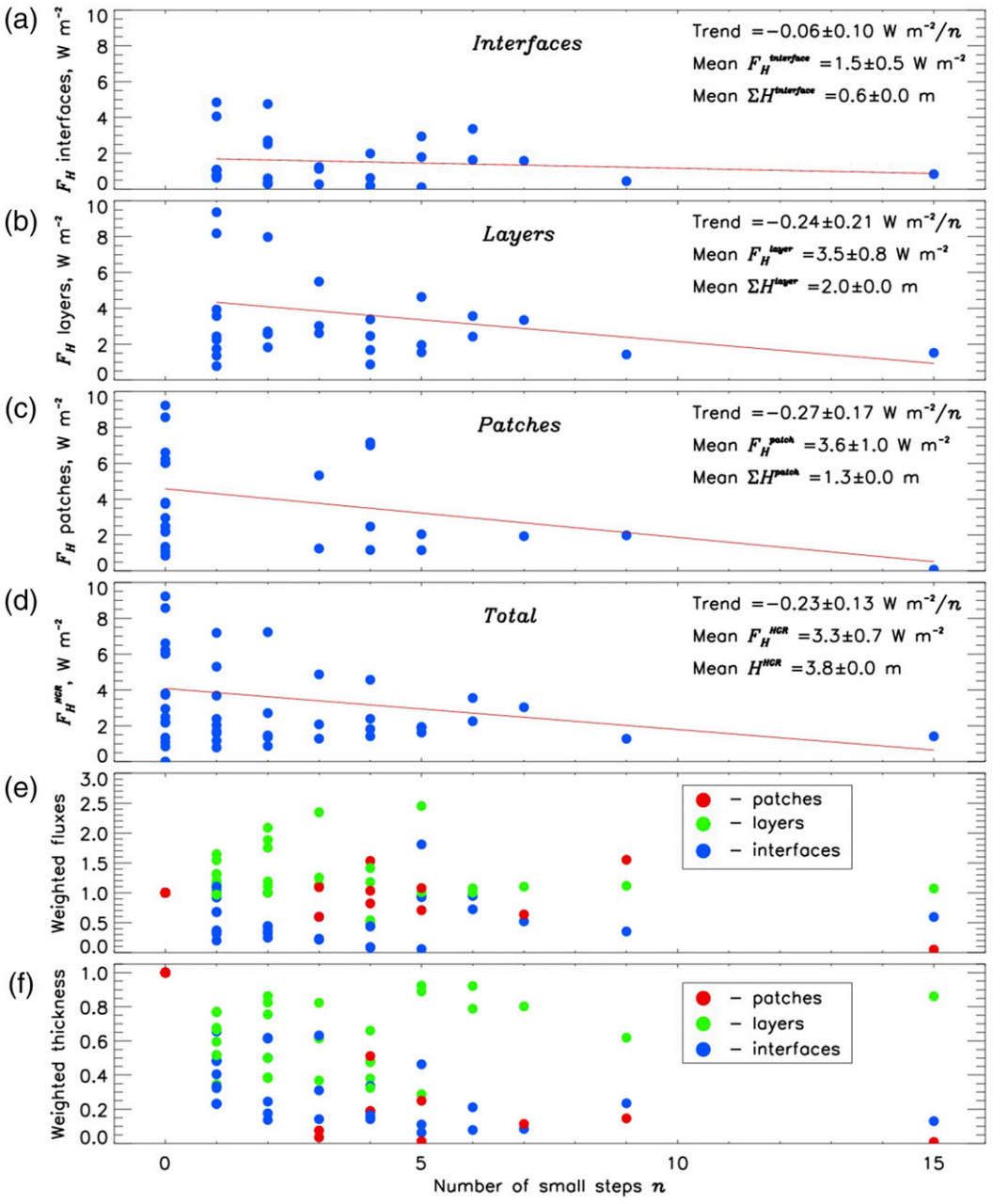

FIG. 7. (a)–(d) Heat fluxes F_H averaged over all small DL interfaces $F_H^{\text{interface}}$ and DL layers F_H^{layer} and over all turbulent patches F_H^{patch} found within each HGR, and the total heat fluxes across HGRs F_H^{HGR} as functions of the number n of small DL steps. Type III HGRs are designated as $n = 0$. Least squares fitted linear trends are shown by red lines. For Type III HGRs, no small DL steps were found within the HGR, and this HGR is considered as a turbulent patch. Estimates of trends, mean heat fluxes, and cumulative thicknesses of interfaces, layers, and turbulent patches within HGR are indicated. (e) Weighted F_H showing (nondimensional) contribution of each component of the HGR to the total F_H^{HGR}. (f) Relative thickness of DL interfaces and layers and turbulent patches (normalized by the thickness of each HGR).

sorted by the three HGR types shown in Fig. 2, shows that these two fluxes have similar means and are significantly correlated (Fig. 8). The mean ratio of HGR-based to layer-based fluxes for each step type varies by about 10%–20%, with ratios of 0.8 ± 0.3, 1.0 ± 0.1, and 1.1 ± 0.2 for Types I, II, and III, respectively (Table 1). The large errors preclude definitive categorization of ratios by interface type.

4. Discussion

The three approaches to calculating heat flux through the large DL steps (section 3) all give similar mean values of ~3–4 W m^{-2} (Table 1). Given that our estimated fluxes are comparable with the value needed to explain the downstream cooling of the AW layer in the eastern Arctic, we conclude that the DL instability is a major contributor to this regional cooling of the AW layer.

In most profiles, however, the region of large steps is overlaid by a staircase of much smaller steps, as seen in Fig. 1b. Fluxes through these small steps are of order 0.1 W m^{-2}, based on thermal microstructure in interfaces that are assumed to carry fluxes by molecular diffusion (Sirevaag and Fer 2012). Therefore, if no other mechanism exists for increasing these fluxes, most of the heat delivered by the uppermost large step to the base of the staircase of small steps cannot escape farther upward. In this situation, the vertical heat flux convergence may broaden the layer of warm AW to the base of the small steps or initiate lateral heat transports within the EB halocline.

Developing methods to represent the DL-driven fluxes in Arctic Ocean circulation models is, therefore, required to improve predictions of AW layer distributions under projected future climates. Here, we discuss conditions that allow for generation of these large steps.

a. Generation and maintenance of large steps

We consider two possible generation mechanisms for the large steps found just above the AW layer throughout much of the EB: 1) convection driven by diapycnal fluxes immediately above the AW layer and 2) homogenization of intrusions.

1) DIAPYCNAL FLUXES

In laboratory experiments, DL layers develop as a salinity-stratified fluid is heated from below. In this case, the heating provides a source of buoyancy that, over time, drives the development of a staircase that can then continue to transport heat through the DL instability even if the original source of heat and buoyancy is removed. A time scale for the development of a layer can be estimated from the heat content change Q required to create a well-mixed layer of height H from an initially linear profile of θ and a temperature change across the resulting HGR after layer homogenization of $\Delta\theta$. For frequently observed values of $H = 25$ m and $\Delta\theta = 0.36$°C, $Q = 0.5\rho c_P H\Delta\theta$ is ~2×10^7 J m^{-2}. With an estimated heat flux of F_H = 3–4 W m^{-2}, it would take of order 1 month to create the first thick layer above the AW core. This time scale is short compared with the ~6–10 months required for AW to be advected in the boundary current along the ~800-km length of the eastern EB slope from St. Anna Trough to the central Laptev Sea at a typical speed of 3–5 cm s^{-1} (Pnyushkov et al. 2015).

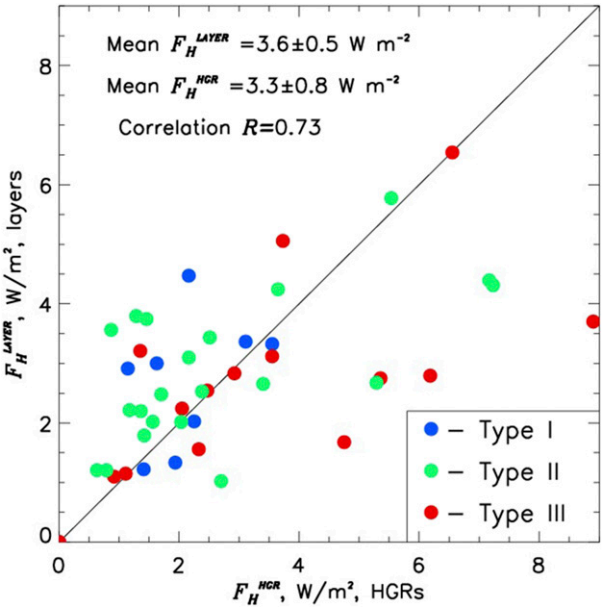

FIG. 8. Comparison of heat fluxes across DL layers and corresponding HGRs, color coded by HGR type. The fluxes are correlated with mean slope of ~1, and the mean fluxes are similar.

The initiation of a DL layer in this manner requires, however, a source of negative buoyancy flux, not simply a heat flux. If the DL instability is initially inactive, then the only other potential source for a strong heat flux from the AW layer is shear instability, but this would be accompanied by a salinity flux consistent with a flux ratio of $R_F = R_\rho > 1$ instead of $R_F < 1$ that is expected for the DL instability (see Kelley 1984, 1990; and section 2). It is possible that instead, the initiation of the DL instability arises through other sources of vertical hydrographic structure and diapycnal divergence of fluxes, including the potential for energetic shear instabilities in regions of strong internal tide generation, within eddies, or as the boundary current of AW interacts with the eastern Arctic continental slope. However, we presently lack the data required to test these speculative hypotheses.

2) INTRUSIONS

Layer heights for the large nearly homogeneous layers studied here are comparable with the vertical length scales of intrusions found in the eastern EB (cf. Figs. 1b,c). Merryfield (2000) proposed that in a region dominated

by salt-fingering stratification, heat and salt flux divergences within intrusions could lead to a stable equilibrium staircase with homogeneous layers and sharp interfaces. Bebieva and Timmermans (2017) carried out a similar study for a DL-dominated stratification in the western Arctic Ocean.

There is some evidence that for given background vertical gradients of θ and S, there is an optimum DL layer height (Kelley 1984, his Fig. 1). The thickness of the layers in the large DL steps discussed here greatly exceeds these predicted optimum values. Kelley et al. (2003) propose that layers split and merge depending on the energetics of layer turbulence relative to stabilizing buoyancy gradients at interfaces. If this conceptual model is correct, then the breakdown of large steps into multiple smaller DL steps (e.g., Figs. 2a,b) is a consequence of weakened convective motion in the overly large layers.

The same heat balance estimates as for the DL instability can be applied to the transformation of intrusions to well-developed convective layers separated by sharp interfaces; time scales are similar and short compared with advective time scales for AW flow along the EB slope. Therefore, based solely on time scales, we cannot distinguish between these two potential mechanisms for generating the large DL layers discussed in this study. However, intrusion dynamics provide a mechanism for initiating vertical variability in stratification that may then interact with external sources of shear (Fig. 3) to create substantial diapyncal fluxes and heat, salt, and buoyancy flux convergences to initiate large DL steps. We tentatively propose that the large DL steps reported here originate from intrusions, possibly where the two flavors of AW—from the boundary current and via the Barents Sea—meet near St. Anna Trough. In this scenario, the large observed values of $\Delta\theta$ across the HGRs are set by the intrusion characteristics. The formation of multiple internal DL steps (examples in Fig. 2) within each Type I and Type II HGR would then be determined by the layer and interface energetics described previously to explain the rough functional relationship between R_ρ and normalized layer heights (Kelley et al. 2003, their Fig. 5) that may be achieved through layer splitting (Kelley 1988).

b. *Limitations of the analyses*

Based on our analyses of 44 microstructure profiles from near the Laptev Sea continental slope (Fig. 1), the Kelley (1990) laboratory-based DL flux formula provides a reasonable assessment of fluxes measured in large DL steps in the eastern EB, provided the fine structure within each HGR is resolved. If, however, the structure of an HGR is underresolved in measurements (e.g., from older CTD measurements), application of the Kelley (1990) flux model to the resolved characteristics of staircases leads to flux estimates that can be an order of magnitude too large. The flux through large steps appears to be relatively insensitive to the structure of these steps, which fall into the three broad categories illustrated by Fig. 2. This observation suggests that characteristics of HGRs adjust to carry a specified flux that is determined by the hydrographic differences between adjacent thick DL layers, consistent with generalized arguments proposed by Kelley (1984, 1988) and other studies. Our data do not allow us to test whether this flux is consistent across the entire EB; it is plausible that the structure of large interfaces varies across the EB depending on other factors such as proximity to sources of mean and time-dependent shear including internal tides.

The noise floor in our microstructure shear measurements corresponds to a lower bound on heat flux of $\sim 2\,\mathrm{W\,m^{-2}}$. Comparisons between fluxes through individual DL interfaces evaluated from microscale thermal gradients, with fluxes in the DL layers from microscale shear, indicate that fluxes through Type I and Type II HGRs clearly exceed this lower bound. However, we cannot use shear-based methods for evaluating DL fluxes through the staircase of small steps that lies above the large steps studied here (Fig. 1b). For these steps, the only approach consistent with available microstructure data is evaluation of laminar (Fickian) fluxes through the interfaces (see Sirevaag and Fer 2012). These studies confirm that fluxes through small steps are low, so that the relatively strong heat fluxes delivered to the top of the set of large DL steps cannot continue upward. However, a bulk heat budget analysis for the central EB by Polyakov et al. (2013) found wintertime heat fluxes through the cold halocline above the staircase of about $3–4\,\mathrm{W\,m^{-2}}$, similar to the flux through the large DL steps just above the AW layer, despite the apparently low fluxes in the staircase of small steps. The Polyakov et al. (2013) study needs to be reconciled with the Sirevaag and Fer (2012) and Kelley (1990) estimates of very low fluxes in the upper thermocline.

One possible mechanism for increasing the flux through the small-steps staircase is the interaction of externally imposed shear with the DL instability (Padman 1994), which relies on shear within the convective layers becoming sufficiently large to create dynamic instabilities of the DL interfaces, so that fluxes through interfaces are turbulent rather than limited to molecular diffusion. The mechanism relies on external shear being significant, but sufficiently low to avoid disrupting the DL layering. Given current limitations on noise levels for shear sensors and resolution of stable

microstructure temperature sensors, observing this mechanism and quantifying its impact on net fluxes requires a measurement program that can simultaneously measure fully resolved interfacial gradients of $\partial T_\mu/\partial z$ and microscale shear magnitude $|u_z|$, and the vertical profile of absolute velocity as a measure of external shear. Multiple profiles would be required, with some profiles at a low fall rate for resolved $\partial T_\mu/\partial z$ ($\sim$0.1–0.2 m s^{-1}; Sommer et al. 2013) and others at a higher fall rate for resolving interfacial shear. Absolute velocity could be obtained from a moored high-frequency ADCP, with the highest-quality data being retrieved from a mooring mounted to sea ice. Alternatively, microconductivity sensors can provide higher vertical resolution of temperature gradients at the present instrument fall speed (Washburn et al. 1996); however, these sensors are sensitive to biofouling and experience large drifts, requiring frequent calibrations to be useful. New microstructure measurements, preferably coincident with observations of external shear, should also cover a larger fraction of the EB since locations of higher flux through the staircase of small steps may not coincide with regions of highest fluxes through the large steps that are the focus of the present study.

5. Conclusions

Using a microstructure dataset from the eastern Arctic Ocean, we have demonstrated that large double-diffusive steps just above the Atlantic Water (AW) layer in the Eurasian Basin (EB) carry substantial vertical heat fluxes, of order 2–8 W m^{-2} with a mean of $\sim$3–4 W m^{-2}, upward from the core of the AW layer via the diffusive layering (DL) instability. These layers are almost ubiquitous throughout the deep water of the EB (see appendix), so that their integrated contribution to cooling and broadening the AW layer in the Arctic Ocean should be substantial.

Detailed examination of high-gradient regions (HGRs) identified in microstructure profiles shows several types of interface structure, ranging from multiple small DL steps to an HGR lacking the characteristics of the DL instability (Fig. 2). These large, complex HGRs are frequently the sites of large microstructure shear magnitude (Figs. 2, 3, 5). This microscale shear might represent either imposed large-scale shear (e.g., from baroclinic tides), as seen in profiles of finescale velocity from a moored profiler (Polyakov et al. 2012; Fig. 3), or enhanced levels of turbulent mixing. Comparisons between turbulent dissipation rate and inferred heat flux through the layers, and shear within the HGRs (Fig. 6), confirm this relationship. The mean ratio of the two estimates of heat flux—one based on layer-averaged dissipation rate and the other on the Kelley (1990) laboratory-based DL formula (flux law) scaled by the number of sublayers—is close to unity for HGRs with visible steps (Table 1), indicating that the flux law gives a reasonable estimate of heat flux, provided the details of the HGRs are adequately resolved.

Our results confirm the previous estimates of DL heat fluxes in the eastern EB based on application of flux laws and show the extent of these features above the AW layer throughout the eastern Arctic. The resulting fluxes in the range 2–8 W m^{-2} are consistent with the estimates of heat fluxes for the bigger steps reported by Lenn et al. (2009). However, these large DL steps are overlaid by much smaller steps suggesting heat fluxes of order 0.1–1 W m^{-2}. That is, although the large DL steps carry sufficient flux to rapidly cool and freshen the AW layer, over much of the EB, we require another mechanism to move this heat from the top of the uppermost large DL layer to the upper ocean where it could affect sea ice volume. Alternatively, this vertical flux divergence may be balanced by strong lateral AW heat fluxes within the Arctic halocline.

Given that DL fluxes above the AW layer can be large, the steps are spatially extensive, and other mechanisms may be able to transport the AW heat to the surface (e.g., Polyakov et al. 2017), we need to further improve our understanding of how DL fluxes will vary as the Arctic Ocean changes through modifications to AW inflow, surface heat fluxes, and freshwater fluxes from precipitation, river inputs, the sea ice annual cycle, and wind-driven export of ice and liquid freshwater (Carmack et al. 2015). This is a challenging goal that can only be achieved by a combination of additional targeted field work, improved parameterizations of DL fluxes that take into account the existing limitations on resolving structures within HGRs, and numerical models for testing the possible complex response of the Arctic Ocean and its sea ice cover to the parameterized DL fluxes.

Acknowledgments. The ship-based oceanographic observations in the eastern EB and Laptev Sea were conducted under the working frame of the NABOS project with support from NSF (Grants AON-1203473 and AON-1338948) and NERC (NE/D005752/1). Analyses presented in this paper are supported by NSF Grants 1249133 and 1249182 and NERC Grant NE/H016007/1. The Ice-Tethered Profiler data were collected and made available by the Ice-Tethered Profiler Program (Toole et al. 2011; Krishfield et al. 2008) based at the Woods Hole Oceanographic Institution (http://www.whoi.edu/itp). VI acknowledges funding from the Ministry of Science and Higher Education of the Russian Federation (Project RFMEFI61617X0076). We thank Jeff Carpenter and two

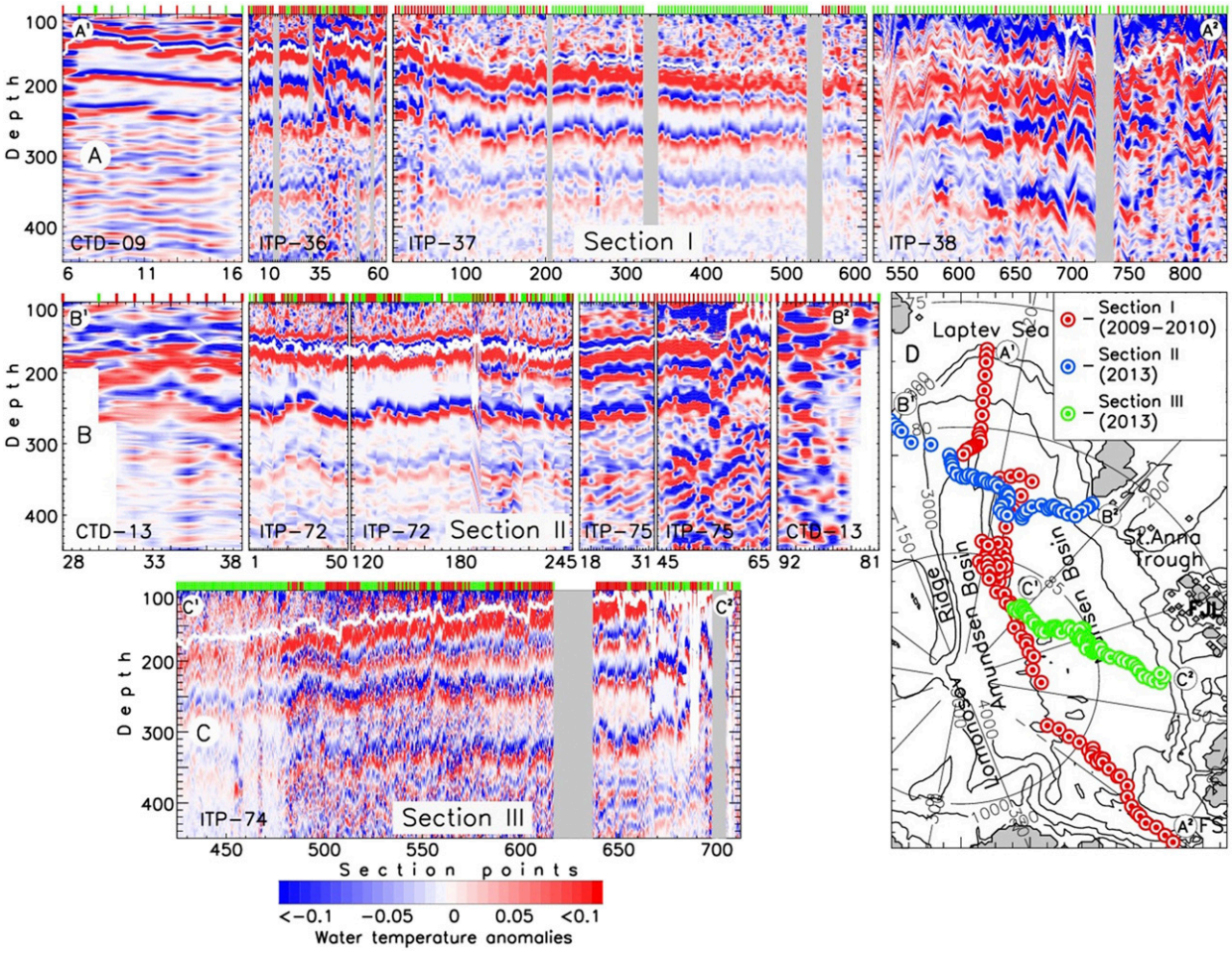

FIG. A1. (a)–(c) Vertical sections (depth; m vs profile number) of potential temperature anomalies (°C) composed from CTD and ITP records. Blue over red stripes identify double-diffusive interfaces or intrusions. Gray vertical segments show missing data. White lines show the position of the isopycnal surface σ_o = 27.80. Red/green segments at the top of the sections identify DL steps (green) and intrusions (red) at σ_o = 27.80. (d) Position of sections; FJL and FS are used for Franz Joseph Land and Fram Strait.

anonymous reviewers for their valuable comments on previous versions of this manuscript.

APPENDIX

Ubiquity of Large DL Steps in the EB

We illustrate the spatial coherence of large DL steps with three transects (locations shown in Fig. A1d) developed using combinations of CTD and ITP data (Fig. A1). For each temperature profile, we applied the method described by Polyakov et al. (2012) to identify DL steps: calculation of a potential temperature anomaly profile $\theta'(z)$ relative to a smoothed profile of $\theta(z)$ generated with a 3-m running average. The choice of 3 m for filter length is based on optimizing the identification of HGRs between thick, nearly isothermal layers. Local negative-over-positive anomalies in $\theta'(z)$ define the upper and lower boundaries of HGRs.

Section I (Fig. A1a) extends >2000 km along the entire EB from the continental slope in the east to Fram Strait in the west, while section II (Fig. A1b) crosses the eastern EB and section III (Fig. A1c) crosses the central Nansen Basin. These composite cross sections demonstrate strong spatial coherence of DL interfaces throughout the EB. Moreover, they show that the spatial pattern has very distinct features between the eastern and central EB from one side and western EB from the other. For example, section I (Fig. A1a) shows very clear DL interfaces in the eastern and central EB (CTD-09, ITP-36, and ITP-37), whereas the record from the western EB (ITP-38) indicates little spatial coherence. Remarkably, interfaces are always found at the same isopycnal surfaces regardless of specific location or time

(e.g., Polyakov et al. 2012). For example, the top of the shallowest thick DL layer in the three transects shown in Fig. A1 is almost always near the depth of the $\sigma_o = 27.80$ isopycnal.

Reduced spatial coherence arises partially from the presence of intrusions [cf. similar measurements from the western Arctic reported by Bebieva and Timmermans (2017)]. The intrusions were distinguished from DL features by checking temperature distributions in both layers above and below an interface (if $\partial\theta/\partial z < 0$ is found, then the structure is identified as an intrusion). As an example, ITP-36 profiles 35–50 in transect I (Fig. A1a) show intrusive vertical structure with no well-mixed DL layers. This is distinct from most other eastern EB profiles where the DL layers are present: hundreds of ITP-37 profiles show the classic DL structure with homogeneous convective layers above and below interfaces. Intrusions are often clustered together (Fig. A1). One cluster is near St. Anna Trough, a region that is famous for its active interactions between the Fram Strait and Barents Sea branches of the AW (e.g., Schauer et al. 1997).

The nearly ubiquitous presence of large DL steps above the AW core throughout the EB (Fig. A1) suggests that if heat fluxes associated with these features are large, they would play an important role in the transformation of AW hydrographic properties as it circulates around the eastern Arctic Ocean.

REFERENCES

Aagaard, K., 1989: A synthesis of the Arctic Ocean circulation. *Rapp. P.-V. Reun. Cons. Int. Explor. Mer*, **188**, 11–22.

Bebieva, Y., and M.-L. Timmermans, 2017: The relationship between double-diffusive intrusions and staircases in the Arctic Ocean. *J. Phys. Oceanogr.*, **47**, 867–878, https://doi.org/10.1175/JPO-D-16-0265.1.

Carmack, E., and Coauthors, 2015: Toward quantifying the increasing role of oceanic heat in sea ice loss in the new Arctic. *Bull. Amer. Meteor. Soc.*, **96**, 2079–2105, https://doi.org/10.1175/BAMS-D-13-00177.1.

Carpenter, J. R., and M.-L. Timmermans, 2014: Does rotation influence double-diffusive fluxes in polar oceans? *J. Phys. Oceanogr.*, **44**, 289–296, https://doi.org/10.1175/JPO-D-13-098.1.

——, T. Sommer, and A. Wüest, 2012: Stability of a double-diffusive interface in the diffusive convection regime. *J. Phys. Oceanogr.*, **42**, 840–854, https://doi.org/10.1175/JPO-D-11-0118.1.

Fernando, H. J., 1987: The formation of a layered structure when a stable salinity gradient is heated from below. *J. Fluid Mech.*, **182**, 525–541, https://doi.org/10.1017/S0022112087002441.

——, 1989: Buoyancy transfer across a diffusive interface. *J. Fluid Mech.*, **209**, 1–34, https://doi.org/10.1017/S0022112089003010.

Flanagan, J. D., A. S. Lefler, and T. Radko, 2013: Heat transport through diffusive interfaces. *Geophys. Res. Lett.*, **40**, 2466–2470, https://doi.org/10.1002/grl.50440.

Gargett, A. E., 2003: Differential diffusion: An oceanographic primer. *Prog. Oceanogr.*, **56**, 559–570, https://doi.org/10.1016/S0079-6611(03)00025-9.

Gregg, M. C., 1987: Diapycnal mixing in the thermocline: A review. *J. Geophys. Res.*, **92**, 5249–5286, https://doi.org/10.1029/JC092iC05p05249.

——, 1999: Uncertainties and limitations in measuring ε and χ_T. *J. Atmos. Oceanic Technol.*, **16**, 1483–1490, https://doi.org/10.1175/1520-0426(1999)016<1483:UALIMA>2.0.CO;2.

——, and T. B. Meagher, 1980: The dynamic response of glass rod thermistors. *J. Geophys. Res.*, **85**, 2779–2786, https://doi.org/10.1029/JC085iC05p02779.

Guthrie, J. D., I. Fer, and J. Morison, 2015: Observational validation of the diffusive convection flux laws in the Amundsen Basin, Arctic Ocean. *J. Geophys. Res. Oceans*, **120**, 7880–7896, https://doi.org/10.1002/2015JC010884.

Hieronymus, M., and J. R. Carpenter, 2016: Energy and variance budgets of a diffusive staircase with implications for heat flux scaling. *J. Phys. Oceanogr.*, **46**, 2553–2569, https://doi.org/10.1175/JPO-D-15-0155.1.

Inoue, R., H. Yamazaki, F. Wolk, T. Kono, and J. Yoshida, 2007: An estimation of buoyancy flux for a mixture of turbulence and double diffusion. *J. Phys. Oceanogr.*, **37**, 611–624, https://doi.org/10.1175/JPO2996.1.

Ivanov, V. V., V. A. Alexeev, I. A. Repina, N. V. Koldunov, and A. V. Smirnov, 2012: Tracing Atlantic Water signature in the Arctic sea ice cover east of Svalbard. *Adv. Meteor.*, **2012**, 201818, https://doi.org/10.1155/2012/201818.

——, ——, N. V. Koldunov, I. A. Repina, A. B. Sandø, L. H. Smedsrud, and A. Smirnov, 2016: Arctic Ocean heat impact on regional ice decay: A suggested positive feedback. *J. Phys. Oceanogr.*, **46**, 1437–1456, https://doi.org/10.1175/JPO-D-15-0144.1.

Kelley, D. E., 1984: Effective diffusivities within oceanic thermohaline staircases. *J. Geophys. Res.*, **89**, 10 484–10 488, https://doi.org/10.1029/JC089iC06p10484.

——, 1988: Explaining effective diffusivities within diffusive oceanic staircases. *Small-Scale Turbulence and Mixing in the Ocean*, J. C. J. Nihoul and B. M. Jamart, Eds., Elsevier Oceanography Series, Vol. 46, Elsevier, 481–502, https://doi.org/10.1016/S0422-9894(08)70566-X.

——, 1990: Fluxes through diffusive staircases: A new formulation. *J. Geophys. Res.*, **95**, 3365–3371, https://doi.org/10.1029/JC095iC03p03365.

——, H. J. S. Fernando, A. E. Gargett, J. Tanny, and E. Özsoy, 2003: The diffusive regime of double-diffusive convection. *Prog. Oceanogr.*, **56**, 461–481, https://doi.org/10.1016/S0079-6611(03)00026-0.

Kolmogorov, A. N., 1941: The local structure of turbulence in incompressible viscous fluid for very large Reynolds numbers. *Dokl. Akad. Nauk SSSR*, **30**, 301–305.

Krishfield, R., J. Toole, A. Proshutinsky, and M.-L. Timmermans, 2008: Automated ice-tethered profilers for seawater observations under pack ice in all seasons. *J. Atmos. Oceanic Technol.*, **25**, 2091–2105, https://doi.org/10.1175/2008JTECHO587.1.

Kwok, R., and N. Untersteiner, 2011: The thinning of Arctic sea ice. *Phys. Today*, **64**, 36–41, https://doi.org/10.1063/1.3580491.

Lenn, Y.-D., and Coauthors, 2009: Vertical mixing at intermediate depths in the Arctic boundary current. *Geophys. Res. Lett.*, **36**, L05601, https://doi.org/10.1029/2008GL036792.

——, T. P. Rippeth, C. P. Old, S. Bacon, I. Polyakov, V. Ivanov, and J. A. Hölemann, 2011: Intermittent intense turbulent mixing under ice in the Laptev Sea continental shelf. *J. Phys. Oceanogr.*, **41**, 531–547, https://doi.org/10.1175/2010JPO4425.1.

Linden, P. F., and T. G. L. Shirtcliffe, 1978: The diffusive interface in double-diffusive convection. *J. Fluid Mech.*, **87**, 417–432, https://doi.org/10.1017/S002211207800169X.

Marmorino, G. O., and D. R. Caldwell, 1976: Heat and salt transport through a diffusive thermohaline interface. *Deep-Sea Res.*, **23**, 59–67, https://doi.org/10.1016/0011-7471(76)90808-1.

Merryfield, W. J., 2000: Origin of thermohaline staircases. *J. Phys. Oceanogr.*, **30**, 1046–1068, https://doi.org/10.1175/1520-0485(2000)030<1046:OOTS>2.0.CO;2.

Onarheim, I. H., L. H. Smedsrud, R. Ingvaldsen, and F. Nilsen, 2014: Loss of sea ice during winter north of Svalbard. *Tellus*, **66A**, 23933, https://doi.org/10.3402/tellusa.v66.23933.

Osborn, T., 1980: Estimates of the local rate of vertical diffusion from dissipation measurements. *J. Phys. Oceanogr.*, **10**, 83–89, https://doi.org/10.1175/1520-0485(1980)010<0083:EOTLRO>2.0.CO;2.

Padman, L., 1994: Momentum fluxes through sheared oceanic thermohaline steps. *J. Geophys. Res.*, **99**, 22 491–22 499, https://doi.org/10.1029/94JC01741.

——, 1995: Small-scale physical processes in the Arctic Ocean. *Arctic Oceanography: Marginal Ice Zones and Continental Shelves*, W. O. Smith and J. Grebmeier, Eds., Coastal and Estuarine Studies Series, Vol. 49, Amer. Geophys. Union, 97–129, https://doi.org/10.1029/CE049p0097.

——, and T. M. Dillon, 1987: Vertical heat fluxes through the Beaufort Sea thermohaline staircase. *J. Geophys. Res.*, **92**, 10 799–10 806, https://doi.org/10.1029/JC092iC10p10799.

——, and ——, 1989: Thermal microstructure and internal waves in the Canada Basin diffusive staircase. *Deep-Sea Res.*, **36**, 531–542, https://doi.org/10.1016/0198-0149(89)90004-6.

——, and ——, 1991: Turbulent mixing near the Yermak Plateau during the Coordinated Eastern Arctic Experiment. *J. Geophys. Res.*, **96**, 4769–4782, https://doi.org/10.1029/90JC02260.

Panchev, S., and D. Kesich, 1969: Energy spectrum of isotropic turbulence from turbulent microstructure. *C. R. Acad. Bulg. Sci.*, **22**, 627–630.

Pnyushkov, A., I. Polyakov, V. Ivanov, Ye. Aksenov, A. Coward, M. Janout, and B. Rabe, 2015: Structure and variability of the boundary current in the Eurasian Basin of the Arctic Ocean. *Deep-Sea Res. I*, **101**, 80–97, https://doi.org/10.1016/j.dsr.2015.03.001.

Polyakov, I. V., and Coauthors, 2010: Arctic Ocean warming contributes to reduced polar ice cap. *J. Phys. Oceanogr.*, **40**, 2743–2756, https://doi.org/10.1175/2010JPO4339.1.

——, A. V. Pnyushkov, R. Rember, V. V. Ivanov, Y.-D. Lenn, L. Padman, and E. C. Carmack, 2012: Mooring-based observations of the double-diffusive staircases over the Laptev Sea slope. *J. Phys. Oceanogr.*, **42**, 95–109, https://doi.org/10.1175/2011JPO4606.1.

——, ——, ——, L. Padman, E. C. Carmack, and J. Jackson, 2013: Winter convection transports Atlantic Water heat to the surface layer in the eastern Arctic Ocean. *J. Phys. Oceanogr.*, **43**, 2142–2155, https://doi.org/10.1175/JPO-D-12-0169.1.

——, and Coauthors, 2017: Greater role for Atlantic inflows on sea-ice loss in the Eurasian Basin of the Arctic Ocean. *Science*, **356**, 285–291, https://doi.org/10.1126/science.aai8204.

Radko, T., 2013: *Double-Diffusive Convection*. Cambridge University Press, 342 pp.

Rippeth, T. P., J. H. Simpson, E. Williams, and M. E. Inall, 2003: Measurement of the rates of production and dissipation of turbulent kinetic energy in an energetic tidal flow: Red Wharf Bay revisited. *J. Phys. Oceanogr.*, **33**, 1889–1901, https://doi.org/10.1175/1520-0485(2003)033<1889:MOTROP>2.0.CO;2.

——, B. J. Lincoln, Y. D. Lenn, J. M. Green, A. Sundfjord, and S. Bacon, 2015: Tide-mediated warming of Arctic halocline by Atlantic heat fluxes over rough topography. *Nat. Geosci.*, **8**, 191–194, https://doi.org/10.1038/ngeo2350.

Robertson, R. A., L. Padman, and M. D. Levine, 1995: Fine structure, microstructure, and vertical mixing processes in the upper ocean in the western Weddell Sea. *J. Geophys. Res.*, **100**, 18 517–18 535, https://doi.org/10.1029/95JC01742.

Rudels, B., E. P. Jones, L. G. Anderson, and G. Kattner, 1994: On the intermediate depth waters of the Arctic Ocean. *The Polar Oceans and Their Role in Shaping the Global Environment*, *Geophys. Monogr.*, Vol. 85, Amer. Geophys. Union, 33–46, https://doi.org/10.1029/GM085p0033.

——, N. Kuzmina, U. Schauer, T. Stipa, and V. Zhurbas, 2009: Double-diffusive convection and interleaving in the Arctic Ocean—Distribution and importance. *Geophysica*, **45**, 199–213.

Schauer, U., R. D. Muench, B. Rudels, and L. Timokhov, 1997: Impact of eastern Arctic shelf waters on the Nansen Basin intermediate layers. *J. Geophys. Res.*, **102**, 3371–3382, https://doi.org/10.1029/96JC03366.

Shibley, N. C., M.-L. Timmermans, J. R. Carpenter, and J. M. Toole, 2017: Spatial variability of the Arctic Ocean's double-diffusive staircase. *J. Geophys. Res. Oceans*, **122**, 980–994, https://doi.org/10.1002/2016JC012419.

Sirevaag, A., and I. Fer, 2012: Vertical heat transfer in the Arctic Ocean: The role of double-diffusive mixing. *J. Geophys. Res.*, **117**, C07010, https://doi.org/10.1029/2012JC007910.

Sommer, T., J. R. Carpenter, M. Schmid, R. G. Lueck, and A. Wüest, 2013: Revisiting microstructure sensor responses with implications for double-diffusive fluxes. *J. Atmos. Oceanic Technol.*, **30**, 1907–1923, https://doi.org/10.1175/JTECH-D-12-00272.1.

——, ——, and A. Wüest, 2014: Double-diffusive interfaces in Lake Kivu reproduced by direct numerical simulations. *Geophys. Res. Lett.*, **41**, 5114–5121, https://doi.org/10.1002/2014GL060716.

Taylor, J., 1988: The fluxes across a diffusive interface at low values of the density ratio. *Deep-Sea Res.*, **35A**, 555–567, https://doi.org/10.1016/0198-0149(88)90131-8.

Timmermans, M.-L., J. Toole, R. Krishfield, and P. Winsor, 2008: Ice-Tethered Profiler observations of the double-diffusive staircase in the Canada Basin thermocline. *J. Geophys. Res.*, **113**, C00A02, https://doi.org/10.1029/2008JC004829.

Toole, J. M., R. A. Krishfield, M.-L. Timmermans, and A. Proshutinsky, 2011: The Ice-Tethered Profiler: Argo of the Arctic. *Oceanography*, **24**, 126–135, https://doi.org/10.5670/oceanog.2011.64.

Turner, J. S., 1965: The coupled turbulent transports of salt and heat across a sharp density interface. *Int. J. Heat Mass Transfer*, **8**, 759–767, https://doi.org/10.1016/0017-9310(65)90022-0.

——, 1973: *Buoyancy Effects in Fluids*. Cambridge University Press, 367 pp.

Walsh, D., I. Polyakov, L. Timokhov, and E. Carmack, 2007: Thermohaline structure and variability in the eastern Nansen Basin as seen from historical data. *J. Mar. Res.*, **65**, 685–714, https://doi.org/10.1357/002224007783649466.

Washburn, L., T. F. Duda, and D. C. Jacobs, 1996: Interpreting conductivity microstructure: Estimating the temperature variance dissipation rate. *J. Atmos. Oceanic Technol.*, **13**, 1166–1188, https://doi.org/10.1175/1520-0426(1996)013<1166:ICMETT>2.0.CO;2.